Distribution Agreement

In presenting this thesis or dissertation as a partial fulfillment of the requirements for an advanced degree from Emory University, I hereby grant to Emory University and its agents the non-exclusive license to archive, make accessible, and display my thesis or dissertation in whole or in part in all forms of media, now or hereafter known, including display on the world wide web. I understand that I may select some access restrictions as part of the online submission of this thesis or dissertation. I retain all ownership rights to the copyright of the thesis or dissertation. I also retain the right to use in future works (such as articles or books) all or part of this thesis or dissertation.

Signature:	
Henry W. Howell	Date

Enhancing the Nonlinear Optical Response in Metasurfaces using Epsilon-Near-Zero Materials

By

Henry W. Howell Master of Science

Physics

]	Hayk Harutyunyan, Ph.D.
	Advisor
W	Vladimir Benalcazar, Ph.D.
	Committee Member
	Sergei Urazhdin, Ph.D.
	Committee Member
	Lili Wang, Ph.D.
	Committee Member
	Accepted:
	Kimberly Arriola
ean of the Jan	nes T. Laney School of Graduate Studies
	Date

Enhancing the Nonlinear Optical Response in Metasurfaces using Epsilon-Near-Zero Materials

By

Henry W. Howell B.S., Emory University, GA, 2022

Advisor: Hayk Harutyunyan, Ph.D.

An abstract of
A thesis submitted to the Faculty of the
James T. Laney School of Graduate Studies of Emory University
in partial fulfillment of the requirements for the degree of
Master of Science
in Physics
2025

Abstract

Enhancing the Nonlinear Optical Response in Metasurfaces using Epsilon-Near-Zero
Materials
By Henry W. Howell

The creation of strong nonlinear optical effects is essential for the advancement of nanophotonic devices. These devices are often limited in efficiency and form-factor due to the high excitation powers and long propagation lengths required by traditional materials. This thesis explores the integration of an ENZ material, indium tin oxide (ITO), into a metasurface geometry with a goal to enhance nonlinear responses, specifically focusing on third harmonic generation (THG). ENZ materials exhibit an array of tunable field enhancement properties stemming from the real part of their permittivity becoming vanishingly small near the ENZ wavelength.

We combine simulations with experimental measurements to design, fabricate, and characterize the ENZ-based metasurface. The proposed metasurface achieved an estimated normalized THG conversion efficiency of $4.18 \times 10^{-9} W^{-2}$; over two orders of magnitude larger than previously published results from a similar metasurface without an ENZ material. Distinct long temporal dynamics were also observed on resonance, further indicating the impact of ITO on the nonlinear response.

The results of this thesis demonstrate the potential of ENZ materials for significantly enhancing nonlinear responses in nanophotonic environments that require high tunability, low excitation powers, and a compact form-factor.

Enhancing the Nonlinear Optical Response in Metasurfaces using Epsilon-Near-Zero Materials

By

Henry W. Howell B.S., Emory University, GA, 2022

Advisor: Hayk Harutyunyan, Ph.D.

A thesis submitted to the Faculty of the James T. Laney School of Graduate Studies of Emory University in partial fulfillment of the requirements for the degree of Master of Science in Physics 2025

Acknowledgments

First, I would like to thank my advisor, Dr. Hayk Harutyunyan, for his continued support, guidance, and expertise throughout my time working with him. I began working with Hayk during my senior year as an undergraduate, which served as my initial introduction to research. After graduating, I continued to collaborate with him on projects, ultimately deciding to return to Emory for my graduate studies to work with him further. I truly cannot thank him enough for the mentorship, encouragement, and opportunities he has provided.

I am also extremely grateful to the members of my lab – Dr. Rabindra Biswas, Yuankai Tang, Xinyu Tian, Sabid Hossain, and Mayrra Sardjito – for their endless support and collaboration. I have learned everything I know about research and laboratory work from this amazing group of people. I couldn't have asked for a better team, they made the challenges of research much more manageable.

I would also like to extend thanks to Mateusz Szurek for all of his help and guidance during my two years in the graduate program. His support and insights have been a huge help to my success.

Thank you to my committee members Wladimir Benalcazar, Sergei Urazhdin, and Lili Wang for your time, guidance, and feedback.

Finally, I would like to thank my girlfriend, family, and friends for their unmatched encouragement and support throughout my time in graduate school and the completion of this thesis. I would also like to give a special thanks to Falafel King in Emory Village for brightening my days and keeping me fueled during long ours of work.

Contents

1	Intr	oducti	ion	1
	1.1	Introduction to Nonlinear Optics		
	1.2	Epsilon-Near-Zero Materials		3
		1.2.1	Drude Model	5
		1.2.2	Drude-Lorentz Model	5
		1.2.3	Electric Field Enhancement, Relaxed Phase Matching, High	
			Dispersion	7
		1.2.4	ENZ Mode and Berreman Mode	9
	1.3	Bound	l States in the Continuum	13
		1.3.1	Symmetry Protected Bound State in the Continuum	15
		1.3.2	Accidental Bound State in the Continuum	17
		1.3.3	True BIC vs. Quasi-BIC	18
	1.4	4 Material and Structure Marriage		
		1.4.1	Combining Intrinsic and Extrinsic factors	20
2	Mat	terial a	and Methods	22
	2.1	Simula	ations	22
		2.1.1	COMSOL Multiphysics and RETICOLO	23
		2.1.2	Simulation Methods	24
	2.2	Exper	imental Methods	26

	2.2.1	Sample Fabrication	26
	2.2.2	Linear Measurements	29
	2.2.3	Nonlinear Measurements	30
	2.2.4	Pump-Probe Measurements	31
3	Results		33
4	Conclusio	n and Next Steps	42
Bi	bliography		44

List of Figures

1.1	Comparison between the Drude model and the Drude Lorentz model	
	for permittivity and refractive index. The blue shaded region is the	
	epsilon-near-zero region, and the red shaded region is the vanishing	
	refractive index region.[26]	(
1.2	Strong dispersion occurs in the ENZ region.[14]	
1.3	Dispersion relation for three film thicknesses. A represents the Berre-	
	man mode, B represents the ENZ mode, and C represents the surface	
	phonon polariton mode. The center vertical line represents the light	
	line. [49]	10
1.4	A three-layer structure containing a layer with thickness d and two	
	semi-infinite regions. [9]	10
1.5	Real part of dispersion relation for short-(red) and long-(blue) range	
	surface plasmon, for different film thicknesses. In the case where the	
	film thickness is smaller than skin depth, the dispersion reaches the	
	plasma frequency. The gray shaded region represents where the mode	
	becomes a large constant electric field inside the film.[10]	1.
1.6	Illustration of wave behavior inside confinement and inside the contin-	
	uum. [22]	1
1.7	Visual describing symmetry-protected BIC in a photonic crystal slab	
	with C_2 rotational symmetry. [22]	16

2.1	Simulated three-dimensional structure. (a) Three-dimensional full unit	
	cell of simulated structure built in COMSOL Multiphysics. Perfectly	
	matched layers are added to top and bottom of structure to simulate	
	real-world conditions, and periodic boundary conditions are applied	
	to simulate array conditions. (b) Close up view of three-dimensional	
	simulated structure with materials labeled	25
2.2	SEM image of final structure with silver back-reflector after etching	
	process. Image supplied by UF Nanoscale Research Facility	27
2.3	Rough Si growth on ITO-on-metal substrate using PECVD. Images	
	supplied by UF Nanoscale Research Facility	29
2.4	Diagram of linear optical path	29
2.5	Diagram of nonlinear optical path	31
2.6	Diagram of pump-probe optical path. [54]	32
0.4		
3.1	Au-dielectric Structure. (a) Side profile illustration of a single unit cell	
	of the Au-dielectric structure. (b) Off-diagonal unit cell of simulated	
	structure in COMSOL. (c) SEM image of final etched sample with gold	
	back-reflector	33
3.2	Comparison between MATLAB and COMSOL reflectance output for	
	Si, ITO pillar on Au. Shows good agreement.	34
3.3	Experimental and Simulated Reflectance Sweeps: (a) Experimental	
	reflectance measurements for Au-dielectric structure. (b) Simulated	
	reflectance for Au-dielectric structure, with ITO ENZ at 1000nm. $$	35
3.4	ITO ENZ Sweep Comparison. (a) ENZ at 800 nm. (b) ENZ at 1000	
	nm. (c) ENZ at 1200 nm. (d) ENZ at 1500 nm. (e) ENZ at 1800 nm.	
	(f) ENZ at 2000 nm	36

3.5	Electric field distribution probing in xz plane, normalized to the inci-	
	dent plane wave: (a) Simulated reflectance sweep for ENZ at $1000nm$,	
	dotted red line shows cut at a diameter of $450nm$ for which electric	
	field distributions were calculated. (b) Magnitude of electric field dis-	
	tribute at $\lambda = 985nm$. (c) Magnitude of electric field distribute at	
	$\lambda=1190nm.$ (d) Magnitude of electric field distribute at $\lambda=1205nm.$	
	(e) Magnitude of electric field distribute at $\lambda = 1350nm$	37
3.6	Electric field strengths in the silicon and ITO pillars. (a) Silicon pillar.	
	(b) ITO pillar	38
3.7	Q-factor analysis: (a) Q-factor overlay for top, middle, and lower re-	
	flectance mode. (b) Q-factor diverging for middle mode	38
3.8	Raw THG counts normalized to background, for changing excitation	
	pump wavelength. The linear reflectance (black line) is overlaid with	
	raw THG data, and the different excitation pump wavelengths (dashed	
	vertical color lines). Highest raw THG counts occurring with pump	
	wavelength of $1215nm$. Pillar diameter is $420nm$	39
3.9	2D map of absorption spectra change (ΔA) as a function of the time	
	delay between the pump and probe and the probe wavelength	40
3.10	Kinetic cuts: (a) Cut at $1190nm$. (b) Cut at $1221nm$	41

Chapter 1

Introduction

This thesis investigates the enhancement of optical nonlinear effects in a metasurface integrated with an epsilon-near-zero (ENZ) material. Specifically, we look at how adding indium tin oxide (ITO) into a resonate metasurface cna enhance third harmonic generation (THG) and change the ultrafast optical dynamics. This approach hopes to address the challenge of producing strong nonlinear signals while avoiding high excitation power and long propagation lengths. This thesis covers the relevant theoretical background, examples of previous metasurface approaches, design and fabrication details, experimental approach, simulation and experimental results, and proposed next steps.

1.1 Introduction to Nonlinear Optics

Most of the time, light-matter interactions involve linear behavior, where a material's response is proportional to the strength of the electric field. In this case, the polarization \vec{P} of a material can be described as:

$$\vec{P} = \epsilon_0 \chi^{(1)} \vec{E} \tag{1.1}$$

However, once the field intensities become high enough, such as the case found near resonances or supplied by a focused laser beam, the linear proportionality begins to break down. Under these conditions, the material responds nonlinearly, opening up the possibilities of many phenomena including intensity-dependent refractive index shifts, frequency conversion, and self-phase modulation. In these cases, the polarization vector \vec{P} becomes a power series in \vec{E} :

$$\vec{P}(t) = \epsilon_0(\chi^{(1)}\vec{E}(t) + \chi^{(2)}\vec{E}^2(t) + \chi^{(3)}\vec{E}^3(t) + \dots)$$
(1.2)

Where $\chi^{(2)}$ and $\chi^{(3)}$ are second- and third-order susceptibility tensors respectively. The second-order $\chi^{(2)}$ term opens the door to effects such as second-harmonic generation (SHG), and the third-order $\chi^{(3)}$ term introduces effects including third-order generation (THG) [7], Kerr Effect, four-wave mixing, and two-photon absorption.

Materials can be described as having inversion symmetry or not. An inversion symmetric material describes a material that is invariant under a point of reflection. Bulk ITO is an example of an inversion symmetric material, where due to its symmetry constraints, the second-order term $\chi^{(2)}$ goes to zero, leaving a non-zero third-order term. One way to break inversion symmetry is by placing the nonlinear material next to other materials or by creating structural asymmetry. Due to the nature of nanostructures, inversion symmetry is often broken allowing for SHG effects. These SHG effects exist only within the boundary regions (i.e., at or near the surface where the interface exists), often resulting in weaker nonlinear responses compared to bulk-related third-order nonlinear effects.

Third-order effects can be further strengthened when dealing with epsilon-nearzero (ENZ) materials such as ITO near the plasma frequency. In this region high $\chi^{(3)}$ is combined with strong electric field confinement which results in significant thirdorder responses. The characteristics of ENZ materials, when paired with structure characteristics make $\chi^{(3)}$ nonlinearities the mechanism of nonlinear effects in these platforms.

The importance of incident light polarization direction on the effect of nonlinearity should be breifly mentioned. The third-order polarization term can be written tensorally as [12]:

$$P_i^{(3)} = \epsilon_0 \sum_{j,k,l} \chi_{ijkl}^{(3)} E_j E_k E_l \tag{1.3}$$

which is a form that shows the influence that vectors and tensors have on the behavior of nonlinear effects. Depending on the system's characteristics and constraints, the realization of nonlinearity may be highly dependent on polarization direction, examples of this often include layered ENZ material structures and metasurfaces [34],[57].

In the following sections, this thesis covers different approaches to enhancing non-linear effects: intrinsic factors such as material properties, specifically large higher-order nonlinear susceptibility χ in ITO, and extrinsic factors such as geometric design, field enhancement, high dispersion, and increasing interaction length. The primary focus is on how combining the benefits of ENZ materials and bound states in the continuum (BIC) can result in a perfect marriage of light confinement and strong nonlinear effects in robust nanophotonic structures.

1.2 Epsilon-Near-Zero Materials

Controlling and engineering the interaction between light and matter lie at the heart of photonics, providing technologies from communication to sensing. Recently, materials exhibiting epsilon-near-zero (ENZ) behavior have received significant attention in the fields of nanophotonics and nonlinear optics, due to their ability to produce novel electromagnetic phenomena that aren't possible with traditional materials. These materials achieve a unique effect in which the real part of their permit-

tivity becomes vanishingly small at select frequencies – typically in the infrared and near-infrared regions – resulting in enhanced nonlinearity, strong field confinement, and unconventional propagation characteristics. This behavior generally occurs at the material's plasma frequency. In thin-film material systems, the ENZ condition can be strongly localized to the interface.

Among the extensive intriguing characteristics of ENZ materials, there are a set of intrinsic and extrinsic factors that contribute to the enhancement of non-linear effects. Intrinsically, many ENZ materials, such as ITO exhibit a large third-order nonlinear susceptibility $\chi^{(3)}$ [1, 30, 36]. Extrinsically, ENZ conditions result in large field enhancement, relaxed phase-matching conditions, and high dispersion, which aid in strengthening nonlinearity and novel light manipulation. The distinction between intrinsic and extrinsic factors is an ambiguous one, and is often context-dependent. However, in this thesis, and in much of the literature, an extrinsic factor can be resultant of material properties, however, must also be possibly achieved by design [14]. For example, slow light condition achieved due to ENZ material characteristics would be considered an intrinsic factor for enhancing nonlinear effects, however, slow light conditions have be achieved through cavity design [20, 37, 6].

To understand and characterize the electromagnetic response and behavior of ENZ materials and why ENZ conditions arise, it's important to first understand the relationship between permittivity and frequency. Permittivity is a material property that describes how a material responds to an applied electric field. This frequency-dependent behavior can be described using the Drude model, which is a classical free-electron model, assuming that electrons can move freely within metals as if they're an electron gas.

1.2.1 Drude Model

The Drude model makes three clear assumptions: electrons scatter at random times and the average time between scattering events is τ , after a scattering event occurs, the average momentum goes to zero after collisions $(\vec{p} = 0)$, and electrons respond to external forces such as the Lorentz force $\vec{F}_L = -e(\vec{E} + \vec{v} \times \vec{B})$ due to their charge -e. We can begin by looking at the equation of motion for a free electron under an external electric field:

$$m\frac{d^2x}{dt^2} + m\gamma\frac{dx}{dt} = -e\vec{E}(t) \tag{1.4}$$

Where x is the electron displacement, m is the mass of an electron, γ is the damping, e is the charge, and the electric field is $\vec{E(t)} = \vec{E_0}e^{i\omega t}$. If we assume $x(t) = x_0e^{-i\omega t}$ and that the induced polarization takes the form of $\vec{P} = -Nex$ (N being the free electron density), then we are left with:

$$\epsilon(\omega) = 1 - \frac{\omega_p^2}{\omega^2 + i\gamma\omega}, \omega_p^2 = \frac{Ne^2}{\epsilon_0 m}$$
 (1.5)

The Drude model does well to describe permittivity dependence on frequency, however, has its limitations since it only accounts for free-electrons, not bound electrons. If accounting for bound electrons is necessary, the Drude-Lorentz model is best.

1.2.2 Drude-Lorentz Model

The Drude-Lorentz model builds off of the Drude model and is a classical model that accounts for bound electrons, treating electrons in the system as damped harmonic oscillators, adding a restoring force. This results in a different equation of motion for the electrons involved:

$$m\frac{d^2x}{dt^2} + m\gamma\frac{dx}{dt} + m\omega_0^2x = -e\vec{E}(t)$$
(1.6)

Here the ω_0 term represents the resonance frequency and is encompassed in the restoring force term. Once solved through, the Drude-Lorentz permittivity takes the form:

$$\epsilon_{DL}(\omega) = 1 + \frac{\omega_p^2}{\omega_0^2 - \omega^2 - i\gamma\omega}, \omega_p^2 = \frac{Ne^2}{\epsilon_0 m}$$
 (1.7)

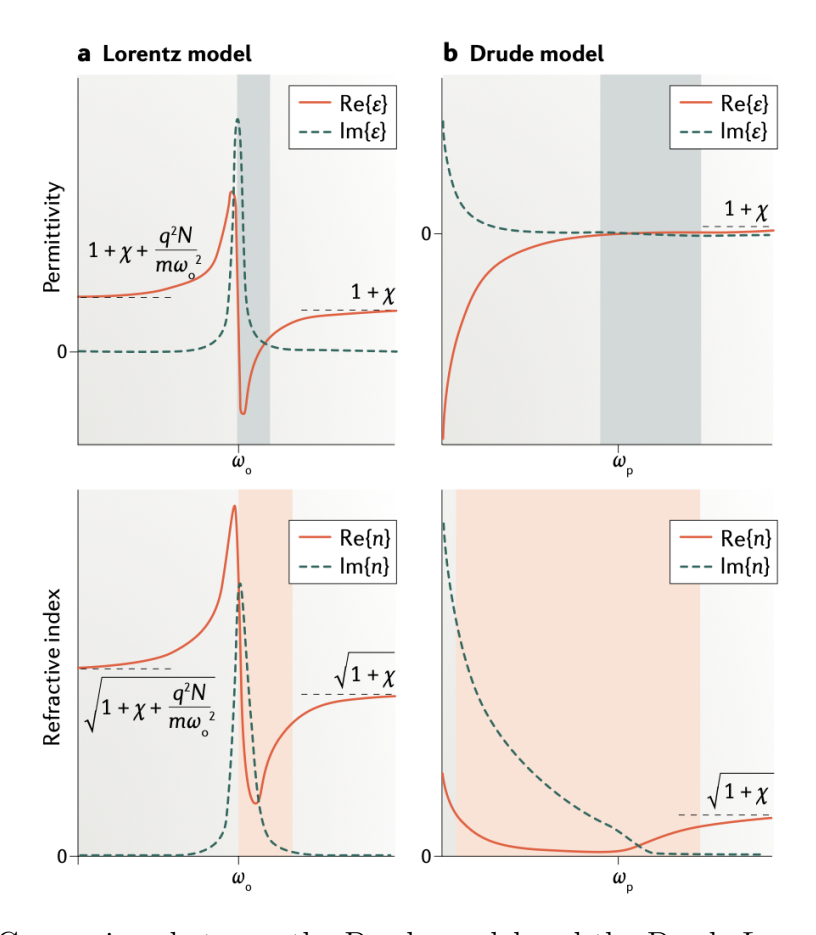


Figure 1.1: Comparison between the Drude model and the Drude Lorentz model for permittivity and refractive index. The blue shaded region is the epsilon-near-zero region, and the red shaded region is the vanishing refractive index region.[26]

1.2.3 Electric Field Enhancement, Relaxed Phase Matching, High Dispersion

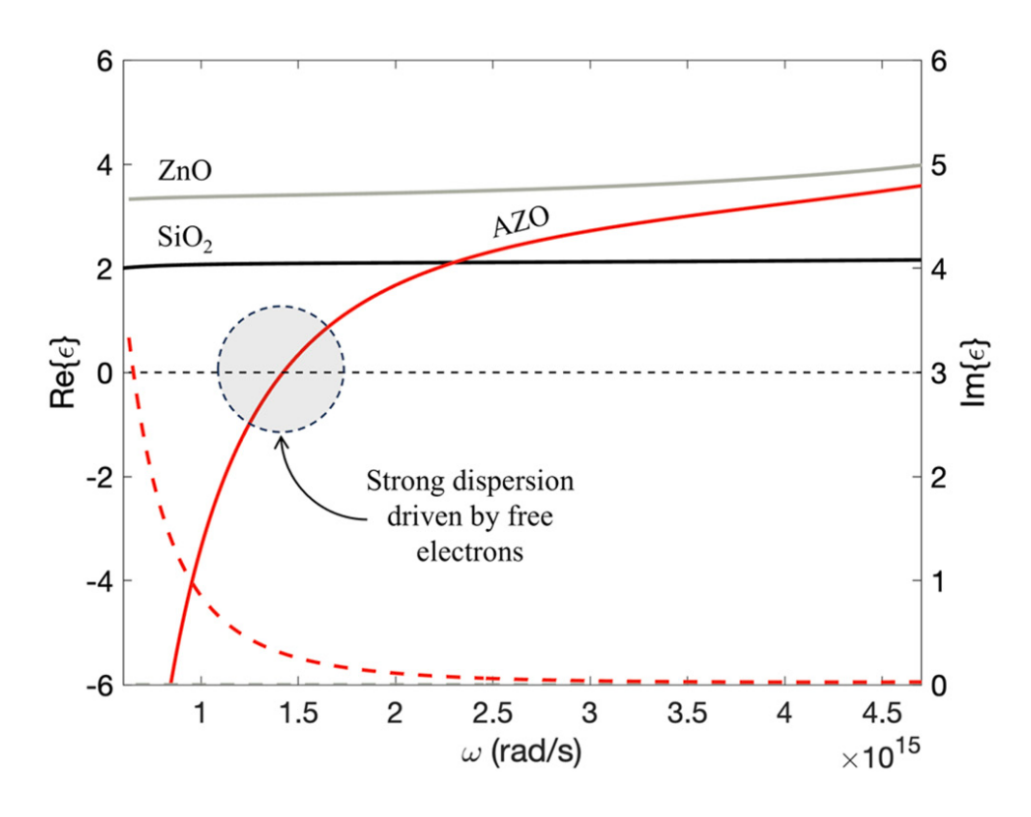


Figure 1.2: Strong dispersion occurs in the ENZ region.[14]

The ENZ condition results in a few notable external factors that contribute to nonlinear enhancement; electric field enhancement, relaxed phase matching, and high dispersion. The electric field enhancement result is the most straight forward advantage and can be easily explained with a few equations. Consider an ENZ material and air interface:

$$\epsilon_{ENZ} E_{z,ENZ} = \epsilon_{Air} E_{z,Air} \tag{1.8}$$

When the real part of ϵ goes to zero (Re[ϵ_{ENZ}] \to 0), the continuity of the normal component of the electric displacement field must be satisfied, resulting in large electric fields in the ENZ material ($E_{z,ENZ} \to \infty$). This enhancement of the electric field

is important because the nonlinear polarization scales like $\vec{P}^{(3)} \propto \chi^{(3)} \vec{E}^3$, so as the electric field \vec{E} increases, the nonlinear effect increases. Due to this being an interface localized effect, it is particularly effective in structures with an ENZ material layer that is thinner than the skin depth [14, 48].

Another noteworthy effect of the ENZ condition is the relaxed phase matching requirements in nonlinear optical processes. Phase matching occurs when interacting waves satisfy momentum conservation, allowing for the generated nonlinear wave to constructively accumulate over the propagation distance. In conventional systems comprised of conventional materials, achieving phase matching is difficult due to short interaction lengths and material dispersion. ENZ materials relax these phase matching conditions as seen below. The permittivity is related to the refractive index as:

$$n_{eff} = \sqrt{\epsilon} \tag{1.9}$$

As $\epsilon \to 0$, so too does the effective refractive index n_{eff} . This has profound consequences, including the wavenumber k going to zero, and the effective wavelength λ tending to infinity as seen below.

$$k(\omega) = -\frac{\omega}{c}n(\omega) \to 0, \lambda_{eff} = -\frac{\lambda_0}{n} \to \infty$$
 (1.10)

In the ENZ regime, the effective wavelength becomes long and the wavenumber becomes small, resulting very slow spacial phase variation. This means that even if the nonlinear and fundamental signals aren't perfectly matching in momentum, they will be able to stay in phase for a longer distance. As a result, ENZ materials support efficient frequency conversion and nonlinear interactions in sub-wavelength structures, conditions that would result in traditional phase matching to fail.

The last notable characteristic of the ENZ region is the high dispersion. Dispersion

is defined as the frequency dependence of a material's permittivity $\frac{d\epsilon}{d\omega}$. In the ENZ region, $Re[\epsilon]$ approaches zero with a sharply bent slope, resulting in a large dispersion relation, as seen in 1.2. This large dispersion has important impacts on group velocity, v_g . The relationship between dispersion and group velocity can be seen explicitly through differentiating the wavevector $k(\omega) = \frac{\omega \sqrt{\epsilon(\omega)}}{c}$. You will find that you're left with a derivative $\frac{dk}{d\omega}$, which is dominated by the term $\frac{d\epsilon}{d\omega}$, resulting in large values of $\frac{dk}{d\omega}$ and a small v_g .

Small group velocity is known as so-called "slow light", which allows for light to spend more time within the material, $\tau_{prop} = \frac{L}{v_g}[14, 6, 25, 26]$, building the nonlinear response.

1.2.4 ENZ Mode and Berreman Mode

Above describes the unique and powerful material responses introduced by the ENZ condition. However, these effects become further pronounced and useful when the ENZ material is placed within a structure that supports electromagnetic eigenmodes. The geometry, boundary conditions, and thickness of the ENZ material layer combine to produce unique confined solutions to Maxwell's equations; so-called "ENZ modes" [49]. These modes showcase dispersion characteristics and field profiles that fall outside the realm of a bulk response, enabling additional light-matter interaction effects.

The ENZ mode is a confined mode that occurs in ultrathin plasmonic or semiconductor films when the real part of the permittivity approaches zero ($Re[\epsilon] \to 0$). Unlike bulk ENZ responses and surface plasmon polaritons (SPPs) that normally occur in thicker materials, ENZ modes are non-radiative eigenmodes, having a dispersion to the right of the light line, as seen in Figure 1.3. They only occur in films with a highly subwavelength thickness, so the mode is vertically confined [9, 10].

Figure 1.4 shows a symmetric three-layer system with an ENZ slab (ϵ_2) sand-

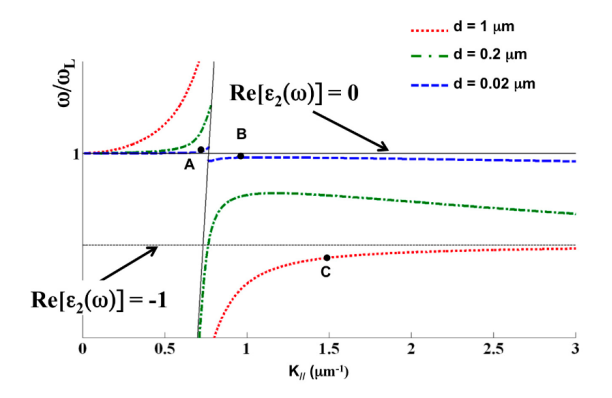


Figure 1.3: Dispersion relation for three film thicknesses. A represents the Berreman mode, B represents the ENZ mode, and C represents the surface phonon polariton mode. The center vertical line represents the light line. [49]

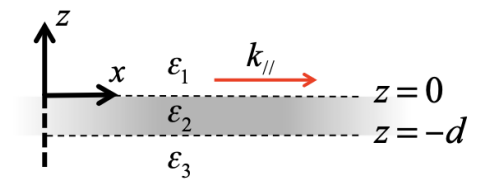


Figure 1.4: A three-layer structure containing a layer with thickness d and two semi-infinite regions. [9]

wiched between two dielectric materials (ϵ_1 and ϵ_3). Any given mode requires the transverse component of its wave vector (k_{\parallel}) and its angular frequency (ω) to satisfy the dispersion equation:

$$1 + \frac{\epsilon_1 k_{z3}}{\epsilon_3 k_{z1}} = i \tan(k_{z2} d) \left(\frac{\epsilon_2 k_{z3}}{\epsilon_3 k_{z2}} + \frac{\epsilon_1 k_{z2}}{\epsilon_2 k_{z1}} \right)$$

$$\tag{1.11}$$

Which can be derived using the three-medium Fresnel coefficient, assuming $Re(k_{zi})+Im(k_{zi}) \geqslant 0$, and applying continuity conditions, and where the longitudinal component (k_{zi}) squared is $k_{zi}^2 = \epsilon_i \frac{\omega^2}{c^2} - k_{\parallel}^2$.

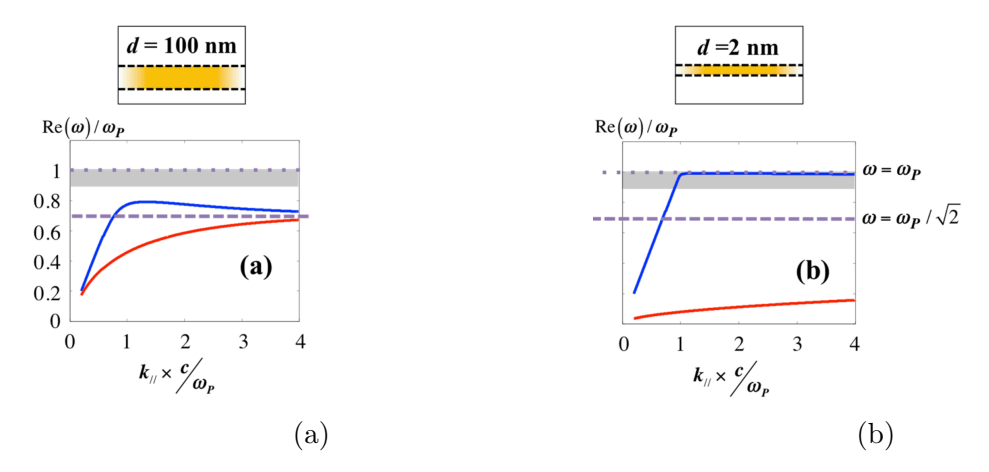


Figure 1.5: Real part of dispersion relation for short-(red) and long-(blue) range surface plasmon, for different film thicknesses. In the case where the film thickness is smaller than skin depth, the dispersion reaches the plasma frequency. The gray shaded region represents where the mode becomes a large constant electric field inside the film.[10]

Figure 1.5 shows the dispersion relations for the short- and long- range surface plasmon within the middle layer. Long-range surface plasmon modes propagate longer distances, on the order of hundreds of micrometers, while short-range surface plasmon modes propagate much shorter distances. When the film thickness is far below the skin depth, the long-range surface plasmon dispersion approaches the plasma frequency, and exists in the conditions that result in a strong, constant electric field within the film. The flat dispersion in the region near the plasma frequency is due to the effective wavelength in the ENZ layer becoming extremely long, creating an essentially

constant field profile within the film. This shows the creation of the ENZ mode.

Under the assumptions that the middle materials is very thin and has a near-zero permittivity, this relation can be approximated as

$$\omega \approx \omega_p \left(1 - \frac{k_{\parallel} d}{4} \right) - i \frac{\gamma}{2},$$
 (1.12)

where ω_p is the plasma frequency, k_{\parallel} is the in-plane wavevector, and γ is the damping rate.

Following from this is an important finding that the longitudinal electric field (E_z) resulting from the ENZ mode is strongly enhanced within the ENZ material as the thickness is decreased. This takes the simple inverse law form:

$$|E_z| \propto \frac{1}{d}.\tag{1.13}$$

The ENZ mode shows large potential for applications requiring enhanced fields within ENZ materials, through combining volume modes and enhancement through reducing film thickness.

A related phenomenon to the ENZ mode is the Berreman mode, which also occurs in ultrathin films at the $Re[\epsilon] \to 0$ point. It differs from the ENZ mode by being a radiative resonance, lying to the left of the light line (Figure 1.3), meaning it can be observed using oblique p-polarized light. It is recognizable by a sharp absorption feature. [4, 41, 18, 13, 49]

In this thesis, indium tin oxide (ITO) is used as the ENZ material because of its highly tunable plasma frequency, large $\chi^{(3)}$, and past experience with it being used in our group. The ITO layer thickness used in this project is 10nm to support the ENZ conditions and modes described above.

1.3 Bound States in the Continuum

BICs provide confined modes without requiring geometrically confining structures, making them a powerful tool in a variety of structures. Before bound states in the continuum (BICs) were experimentally realized, electric-field confinement in nanostructures was achieved through techniques such as the use of mirrors or geometrically enclosed structures that limit the amount of external coupling.

BICs are a resonant mode that exists within the continuum of radiative modes, while remaining decoupled from them. This allows the BIC mode to remain localized without radiating. Originally proposed by Neumann and Wigner in 1929 [40], and first experimentally realized by Chia Wei Hsu et al. in 2013, through the use of photonic crystal slabs [23], the concept has recently grown in popularity in the optics community due to its ability to enhance fields in nanostructures. In the context of nonlinear optics, BICs offer a powerful extrinsic mechanism for enhancing optical nonlinear effects. BICs result in strong field confinement that increases the local field intensity within the materials, in turn enhancing nonlinear processes such as harmonic generation, optical Kerr effects, and four-wave mixing [55] [52] [38] [3].

Classical wave theory defines two distinct spectral wave behaviors, bound and radiative depending on their frequency. If the frequency of the wave falls outside the range of the continuous spectral region, then it is considered a bound, non-radiating wave. However, if a wave has a frequency that falls within the continuous spectral region, then it is a radiative wave. BICs break this classic mold by existing within the continuum while remaining fully localized and non-radiative. Figure 1.6 shows a visualization of these spectral behaviors. This illustration assumes a time-dependent sinusoidal oscillating wave with the form $e^{-i\omega t}$, where t is the time and ω is the frequency. Starting from the bottom, the green frequency is a conventional bound state, existing in a realm with discrete energy levels outside of the continuous spectrum. No radiation occurs for these bound states. This can be thought of in the

context of bound electrons of an atom, where they can only occupy quantized energy levels. Moving up, the blue frequency represents wave behavior within the continuum, where the energy levels aren't quantized and the energy is radiated out to infinity. Next, the orange frequency represents a resonance mode within the continuum. There exists a localized component, but the mode is coupled to propagating waves within the continuum which results in the leakage of the mode. The frequency of these leaky modes can be described as $\omega = \omega_0 - i\gamma$ [56] [22], where the imaginary part $-\gamma$ describes the mode's decay rate, directly relating to its Q-factor, which is defined as $Q = \omega_0/(2\gamma)$. The Q factor diverges as $\gamma \to 0$, resulting in vanishingly small loss, thus long-life modes. Finally, the red frequency represents the bound state in the continuum mode where there is no coupling to the propagating waves in the continuum, so there is no leakage. This represents a true BIC, where the γ is zero, theoretically allowing infinite Q-factors.

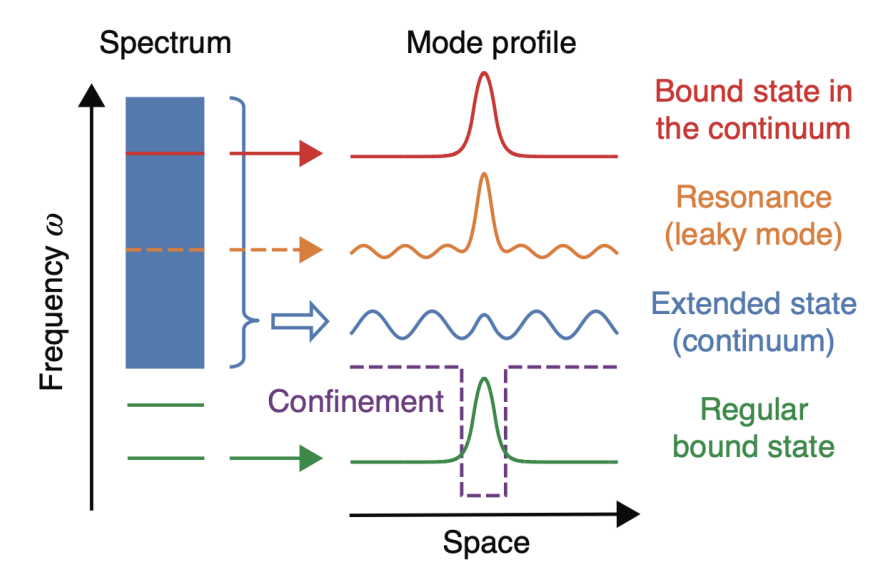


Figure 1.6: Illustration of wave behavior inside confinement and inside the continuum. [22]

Now that the basic picture of a BIC is established, we can explore the mechanisms through which BICs are formed. The two most prominent forms of BICs are symmetry protected and mode interference, or accidental BICs. Symmetry protected BICs

are where the BIC mode is restricted from coupling to radiative channels due to the physical symmetry of the structure. Mode interference BICs, such as Friedrich-Wintgen BICs (FW-BICs), are due to the destructive interference between two leaky modes which results in the radiation being canceled out completely.

1.3.1 Symmetry Protected Bound State in the Continuum

One of the most studied mechanisms for realizing bound states in the continuum is symmetry protection, where the non-radiative nature of the BIC arises from a mismatch in symmetry between the spatial profile of the mode and the available radiation channels [35]. Electromagnetic coupling requires overlap in both spatial and symmetry properties, so a mode that does not share the symmetry of the outgoing radiation cannot couple to it, and thus remains localized.

This effect is often realized in periodic structures, such as photonic crystal slabs or metamaterial arrays [19, 51, 23]. At the Γ -point (the center of a Brillouin zone), the structure supports modes with well-defined symmetry, for example even or odd parity with respect to the mirror planes in the unit cell. The external radiation field generally has less abundant symmetry forms. When the guided mode's symmetry is incompatible with the free-space radiation mode's, the overlap integral between the two vanishes, resulting in zero radiation loss. In this case, the mode becomes invisible to the continuum because there is no way for it to leak energy, even though it exists at a radiative frequency.

To provide a more explicit explanation of symmetry mismatch, lets consider a photonic crystal slab that is mirror symmetric about a middle horizontal plane (z = 0), similar to the structure featured in [23]. This system is invariant under mirror reflection, which means it doesn't change by the transformation $z \to -z$. As a consequence of this, the modes can be described by their parity under this reflection, leaving us with field profiles in the form of $E_z(x, y, -z) = E_z(x, y, z)$ (Even), or

$$E_z(x, y, -z) = -E_z(x, y, z)$$
 (Odd).

Symmetry-protected BICs arise when there is a resonant mode supported by the slab that is odd with respect to the mirror plane, and the available radiation modes in the continuum are even. Since the two modes have different symmetry, the overlap integral goes to zero:

$$\int E_{rad}(x, y, z) E_{BIC}(x, y, z) dV = 0, \qquad (1.14)$$

resulting in a localized, confined mode in the continuum.

An important aspect of symmetry-protected BICs is their high sensitivity to structural perturbations [33]. Any breaking of the underlying symmetry – such as fabrication imperfections, off-normal incidence, or intentional geometric asymmetry – enables coupling to the continuum and turns the BIC into a quasi-BIC with a finite Q-factor.

c Photonic crystal slab

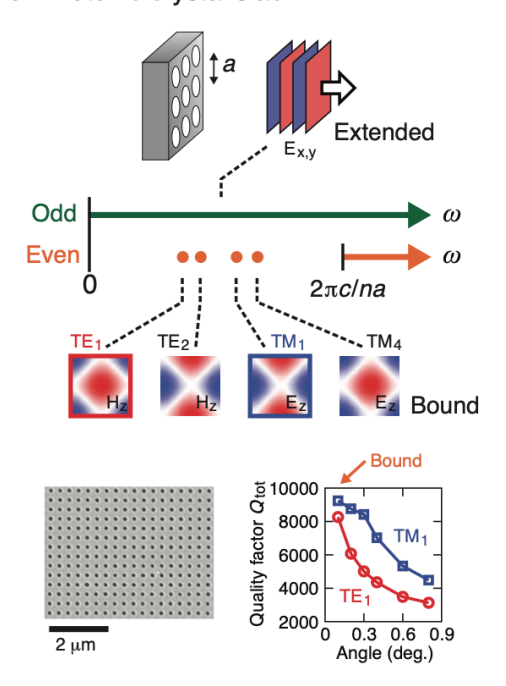


Figure 1.7: Visual describing symmetry-protected BIC in a photonic crystal slab with C_2 rotational symmetry. [22]

Figure 1.7 shows a structure similar to the structure discussed above, however, the symmetry arises from a C_2 rotation symmetry around the vertical center axis. On the top left is the slab with periodic placed hole. At the Γ -point, at normal incidence, the radiation modes have odd parity under the 180° rotation, while select modes (such as TM_1 and TM_4) in the slab are even. This mismatch in symmetry is what forbids coupling and results in a symmetry-protected BIC.

The green horizontal line labeled "Odd" represents the large range of slab modes that are of odd-parity. They are modes that can couple to radiation channels that are also odd under C_2 , producing leaking modes. This is contrasted by the orange dots labeled "Even" which describe the slab modes that are even under the rotation and can't radiate, remaining bound at the Γ -point, resulting in symmetry-protected BICs. The bottom right shows the Q-factor comparison between the TM_1 and TE_1 modes as the wavevector moves away from the Γ -point. Away from the Γ -point, the Q-factor becomes finite due to the symmetry protection being lifted, and the entering into the quasi-BIC regime.

1.3.2 Accidental Bound State in the Continuum

Accidental BICs differ from symmetry-protected BICs because they come about through the destructive interference between two or more leaky resonant modes, instead of from a symmetry mismatch with the radiation continuum. Among accidental BICs, the Friedrich-Wintgen BICs (FW-BICs) are the most well-known. They were first introduced in the context of quantum systems in 1985 by Friedrich and Wintgen [15]. FW-BICs do not require any geometric symmetry because they arrise due to interference between existing radiative modes in the system.

In photonic systems, FW-BICs generally arise from the far field destructive interference of two resonant modes with similar frequency and symmetry. In these systems, individual modes couple to radiation channels and leak energy. Normally, these radiation channels would result in the energy propagating to infinity, however, in the case of FW-BICs, the radiation channels interfere with each other forbidding outgoing waves. This results in a non-radiative state, even when the individual modes satisfy the usual conditions for radiation.

Unlike symmetry-protected BICs, which are confined to high-symmetry points like the Γ point, FW-BICs do not require structural symmetry and can occur away from the Γ point [33]. This opens up more design flexibility for photonic devices in a field where spatial and spectral control over field enhancement is important. Although FW-BICs offer greater design freedom, they still require tuning of structural parameters to achieve the conditions required for radiation cancellation. Tunable parameters can include thin-film thickness, unit cell periodicity, and material refractive indices.

In the context of this thesis, the structure is designed to support accidental BICs instead of than symmetry-protected. This allows for more freedom in both the design and fabrication processes, avoiding the necessary perfect structural symmetry or polarization control that comes along with symmetry-protected BICs. Using interference-driven BICs means the system can achieve strong field confinement while remaining robust to fabrication imperfections and accessible under normal incidence, making it perfect for experimental realization.

1.3.3 True BIC vs. Quasi-BIC

Although BICs offer perfect field confinement, their true decoupling from the continuum makes them impossible to access. This lack of coupling to outgoing radiation modes makes it so they cannot be directly observed or measured through transmission or reflection. This creates a kind of paradox: although BICs are perfect at confinement and trapping energy in the system, they do it so well that it limits their practical uses immensely.

In order to make BICs and their benefits useful in the real world, a less than perfect

BIC needs to be created. This is effectively called a quasi-BIC state and is formed through the intentional introduction of perturbations in the system. Quasi-BICs retain the fundamental characteristics of BICs, such as the strong field localization and high Q-factors, but have finite lifetimes and non-infinity Q-factors due to their slight radiative leakage. This leakage, while negatively impacting confinement, is a necessary evil to enable light coupling and non-linear signal extraction.

There are essentially infinite ways to transition a true BIC to a quasi-BIC, however the most common methods are through symmetry breaking, tuning of geometric parameters, and off-normal excitation. Breaking symmetry in a system that produces symmetry-protected BICs allows for coupling that was previously not allowed, resulting in a non-perfect BIC condition, or a quasi-BIC. For example, in metasurface arrays comprised of cylindrical pillars, changing the circular pillar to a more elliptical shape breaks the in-plane mirror symmetry, thus allowing coupling to the continuum [33, 43]. This concept has also been applied to arrays of rectangles [28] and rings [5]. Another way to transition from true BIC to quasi-BIC is by altering the structural parameters in a way that de-tunes the interference that results in a FW-BIC. For example, changing the spacer thickness between a nanostructure and its mirror image alters the radiation interference [53]. Similarly, changing parameters such as the pillar diameter can alter the interference patterns within the structure [45]. Lastly, exiting a system at a nonzero in-plane wave vector can result in transitioning a true BIC to a quasi-BIC. Many BICs exist at the Γ point, and by exciting at a nonzero in-plane wave vector, the symmetry conditions are lifted and a quasi-BIC results.

In nonlinear optics, both field confinement and radiative coupling are essential, and neither is very useful without the other. Quasi-BICs represent the best of both worlds. They support large local field enhancement while still allowing efficient coupling of nonlinear signal to outgoing radiation channels.

1.4 Material and Structure Marriage

1.4.1 Combining Intrinsic and Extrinsic factors

In order to achieve the strongest most robust nonlinear responses, a careful marriage of both extrinsic and intrinsic enhancement mechanisms must be achieved. This approach typically involves choosing materials with high intrinsic nonlinear susceptibility – as discussed in the nonlinear section above – and taking advantage of materials' ENZ condition to elicit unique phenomenon. These can be complimented and supported by choosing a geometry that introduce extrinsic mechanisms that confine modes and enhance fields.

A prime example of this approach is shown by P. Xie et al. [51], who developed a Si-ITO metasurface consisting of an ITO thin-film with a symmetry-breaking Si structure on top. This design pairs the strong inherent nonlinear susceptibility and ENZ conditions of ITO with the enhanced confinement brought in by the symmetry-protected BIC, producing nonlinear coefficients that are over three orders of magnitude higher than that of unpatterned ITO.

Similarly, G. Yang et al. [53] created a Si-Si O_2 structure composed of a Si pillars on a Si O_2 spacer layer on a gold mirror. This structure combined the nonlinear susceptibility of Si with a accidental BIC to enhance nonlinearity. This approach is intriguing, because it produced a BIC condition without breaking geometrical symmetry, but through tuning the coupling between the Si pillar's MD mode and it's mirror image in the gold mirror. By changing the separating layer thickness, the coupling was controlled and a Quasi-BIC condition was achieved.

A further evolution of this approach was then taken by W. Shi et al. [45] who swapped the SiO_2 separating layer out for an ITO pillar. This change retains the BIC-producing geometry while introducing an ENZ nonlinear material in the vicinity where the field confinement occurs. This approach theoretically results in increased

nonlinear enhancement due to an increased electric-field density within the ITO pillar, however, it hadn't been experimentally explored.

Intrigued by this approach, the goal of this thesis is to experimentally investigate whether such a structure results in enhanced nonlinear optical effects. More specifically, we explore a layered ITO-based metasurface with a gold back-reflector and symmetry-preserving resonator. The aim is to effectively leverage both intrinsic material related nonlinearities and extrinsic ENZ conditions and mode-confinement techniques. This hybridized design seeks to marry material and structural optimization to push light-matter interactions in the nanophotonic scape.

Chapter 2

Material and Methods

2.1 Simulations

To achieve the strongest light-matter interactions for nonlinear effects, simulation software was used to guide the design and analysis of the structure studied in this work. Identifying optimal geometry and material parameter pairing is essential for strong nonlinearity, however, experimentally investigating this over multiple renditions takes a lot of time and money. Simulations address these time and money constraints while offering accurate results that are easily implemented into the real-world experimental space. COMSOL Multiphysics and MATLAB with RETICOLO [24] are the simulation software used in this work to simulate reflectance, transmission, absorption spectra, and characterize modes. Each software package offers reliable simulation results, however, uses different solving methods, resulting in distinct advantages – COMSOL is best used for complex geometries where full-field electromagnetic analysis is needed and RETICOLO is best for simpler periodic structures and spectral analysis where quick results are valued.

2.1.1 COMSOL Multiphysics and RETICOLO

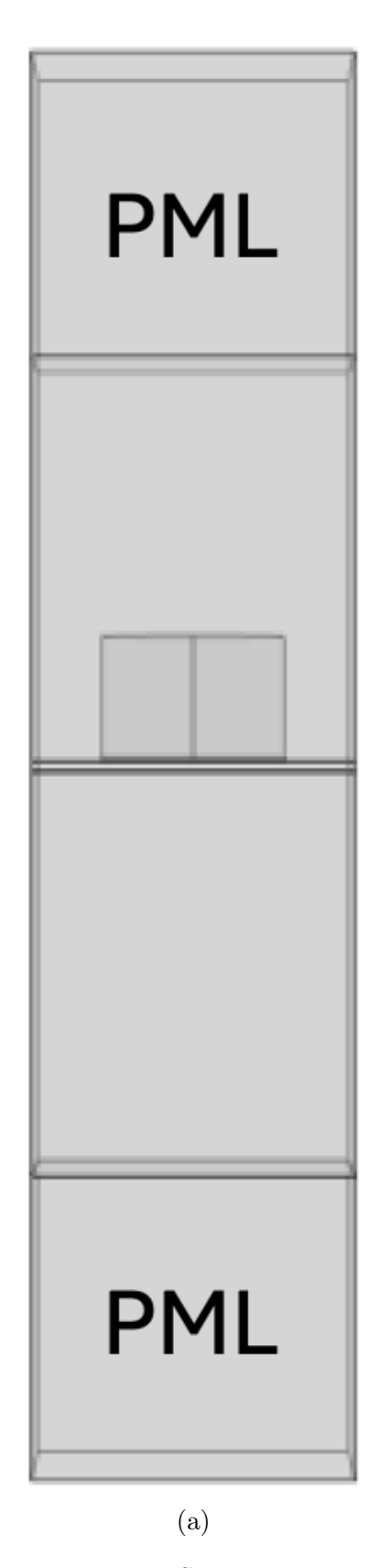
COMSOL Multiphysics uses finite element method (FEM) for solving models. FEM works by breaking a physical problem into smaller finite elements to help tackle solving. A grid, called a mesh, is created that consists of elements connected by nodes. Values are found at the nodes and used to approximate the values across the element by creating differential equations for each element. These sets of equations are then solved to give a solution for the global system. [21, 39, 42, 2] RETICOLO uses rigorous coupled-wave analysis (RCWA) to solve models. This method only works with periodic structures and takes advantage of this periodicity when solving. Since the structure is periodic, the electromagnetic fields and permittivity can be expanded in terms of a Fourier series. This expansion simplifies the computation immensely by breaking down continuous variations in the form of Maxwell's equations into a system of coupled differential equations in Fourier space. [46, 24] The Fourier components can then be separated by a matrix that describes how the system evolves along the direction of propagation, and ultimately solved as an eigenvalue problem. [21]

The use of both rather than just one comes down to their limitations. COMSOL Multiphysics is much more computationally taxing and requires larger computational power and time. RETICOLO on the other hand is less computationally taxing, allowing for simulations to be run on personal computers rather than computing stations in a faster time frame. Since this work's structure is a relatively simple, periodic structure, both software could be used for accurate results. RETICOLO was used for the first line of investigation, plotting large reflectance sweeps for rough initial designing and characterization of the structure. Once large sweeps were created, COMSOL was used to run single diameter spectra calculations, spacial electric field distributions, and identify field confinement.

2.1.2 Simulation Methods

Figure 2.1a shows a three-dimensional visual of a single unit cell built in COMSOL Multiphysics, Figure 3.1b shows a zoomed in image of the pillar structure. This structure was modeled in both COMSOL Multiphysics and RETICOLO. Periodic boundary conditions were used in the x and y directions to simulate it's infinite periodicity in the xy-plane. Perfectly matched layers were placed above and below the structure, as seen in Figure 2.1a, to minimize non-physical light behavior due to simulation boundaries. These were paired with scattering boundary conditions to further ensure simulation boundaries wouldn't produce artificial interference effects. A fine physics controlled mesh was used in COMSOL simulations, and an order of [20, 20] Fourier components was used in RETICOLO. Refractive index data for gold, and silicon was measured and supplied by the lab, silicon dioxide (glass) data was supplied by L. Gao [16], and the Cr data was supplied by A. Sytchkova [47]. ITO optical data was the trickiest to produce due to it's high tunability. A MATLAB script using the Drude model was used to produce refractive index data when supplied a γ, ω_p , and ϵ_{∞} . This approach allowed for the generation of ITO refractive index tailored to the target ENZ wavelengths prior to fabrication. Once fabrication was complete, RETICOLO was used to fit simulated reflectance spectra to experimental linear data to extract the experimental structure's ITO ENZ wavelength.

The simulation process largely followed a workflow that mirrored the design and experimental validation phases. First, the rough design of the structure and desired materials were determined by gauging the literature. Next, initial large-sweep reflectance spectra were simulated using RETICOLO to identify resonant features and how they change with structural changes, such as pillar diameter or material thicknesses. The features and their behavior were analyzed by looking at literature on ENZ materials and BIC conditions. After identifying modes that seem promising for producing BICs, COMSOL was used to confirm linear spectrum results for individual



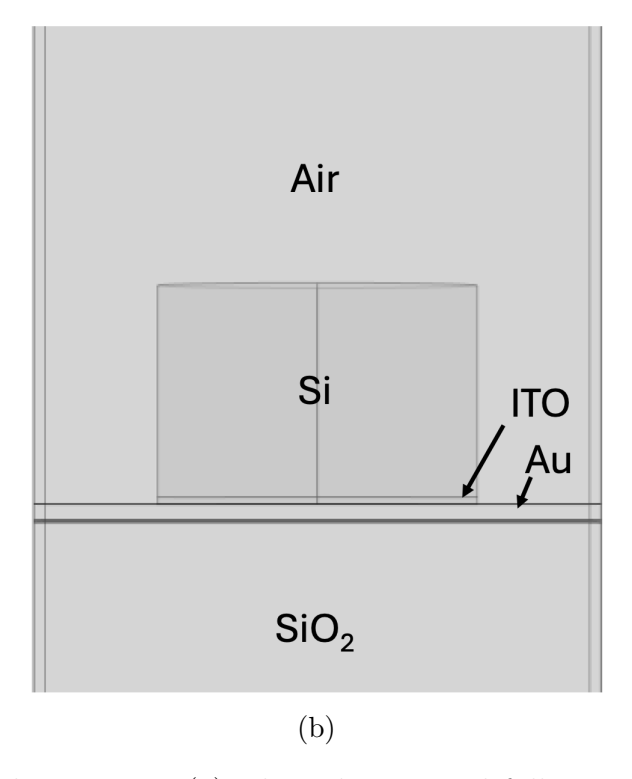


Figure 2.1: Simulated three-dimensional structure. (a) Three-dimensional full unit cell of simulated structure built in COMSOL Multiphysics. Perfectly matched layers are added to top and bottom of structure to simulate real-world conditions, and periodic boundary conditions are applied to simulate array conditions. (b) Close up view of three-dimensional simulated structure with materials labeled.

diameters, and to visualize the spacial electric field distributions at points of interest. Electric field distributions were particularly useful in determining the origin of modes, and to show confinement in ITO.

Once sample fabrication was complete, the ITO ENZ was unknown, so RETI-COLO, transverse matrix method (TMM), and Drude model were used to fit simulation reflectance to experimental while sweeping ITO plasma frequency (ω_p) with a constant ϵ_{∞} and γ values based on literature [32]. This helped determine a relative ENZ of the fabricated ITO, allowing simulations that matched the experimental results and this characterization of the experimentally realized modes.

2.2 Experimental Methods

2.2.1 Sample Fabrication

Fabrication began with dialing in the ITO thin film recipe on glass. Glass cover slides were cut in half using a diamond tipped pen, pieces were marked with a letter "R" on the side that experienced the cutting. The glass was then cleaned using sonication for rounds of soapy water, acetone, and isopropyl alcohol (IPA), before being covered and stored in IPA. Radio frequency (RF) magnetron sputtering was used to sputter 10nm of ITO on the glass substrates. All deposition occurred on the working surface; the side opposite of the side marked "R". This is to avoid contamination caused by glass particle over-spray resulting from the cutting procedure. Power is 50W, argon flow was kept at a flow of 12.0SCCM during sputtering, and chamber base pressure reached $2 \times 10^{-7} Torr$ before introducing argon gas. Base pressure was kept consistent and low to keep chamber oxygen content consistent and low. Oxygen flow during ITO sputtering has been shown to impact ITO material parameters and physical properties [27, 50, 11]. Sputtering rates were varied from 6.2 Å/s to 2.5 Å/s. Thermal annealing was used to tune the ITO's ENZ by altering the oxygen vacancies

within the ITO, and in turn altering the ITO's free carrier concentration. Longer durations of time at the target temperature, resulted in more oxygen atoms being stripped from ITO, leaving behind more free carriers in the ITO, and blue shifting the ENZ frequency. An annealing recipe was developed that consistently produced an ITO with a target ENZ frequency.

Once the ITO behavior had been dialed in, fabrication progressed to the ITO-on-metal substrates. Substrates with both gold and silver back-reflectors were used, however the final design only involved samples with gold back-reflectors. The sample made with a silver back-reflector experienced extensive degradation and pitting during the etching process, ultimately making it unusable. Figure 2.2 shows the severe damage it exhibited.

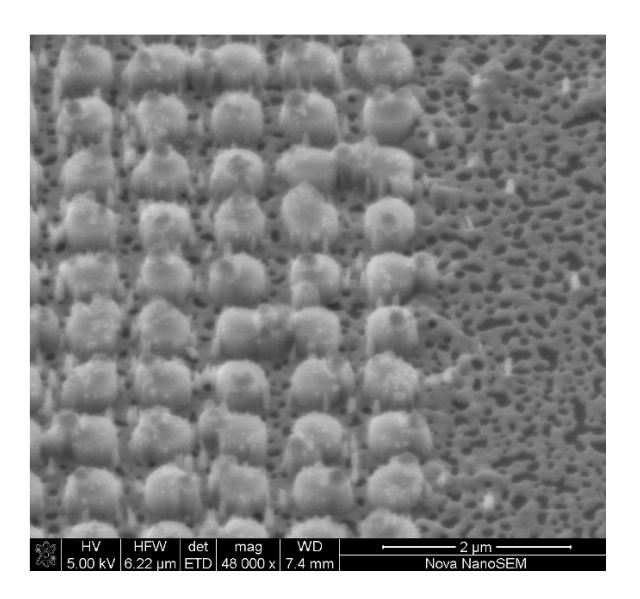


Figure 2.2: SEM image of final structure with silver back-reflector after etching process. Image supplied by UF Nanoscale Research Facility.

Thermal evaporation was used to deposit a 3nm chromium adhesion layer $(0.5\text{\AA}/s)$, before depositing 23nm of gold $(0.5\text{\AA}/s)$. Again, RF magnetron sputtering was used to sputter 10nm of ITO on top of the gold. Film thickness and uniformity were verified using atomic force microscopy (AFM). The fabricated ITO-on-Au substrate was then annealing according to the recipe determined earlier. Following the ITO-on-

Au substrate fabrication and annealing, reflectance measurements were performed to verify the ITO ENZ frequency. No such feature indicating the ITO's ENZ could be located in the reflectance spectra. Literature and work function analysis suggest that by growing ITO on metal, such as gold, the ITO could borrow free carriers from the gold. In a study where varying thicknesses of ITO films were placed on 5nm of gold [29], the carrier concentration of the ITO was shown to increase dramatically as the ITO thickness to gold thickness ratio diminished. This increase in carriers results in the ITO's ENZ frequency to substantially blue shift without the need of post-sputter annealing. Additionally, the same study shows that gold has a large effect on the crystalinity of ITO grown on top of it, further impacting the material characteristics. Ultimetly, this project's ITO-on-Au substrates weren't annealed, and the ENZ frequency was still not able to be measured using the previously effective optical setup. Setup error was ruled out by depositing gold on top of ITO with a known ENZ frequency. Taking reflectance measurements through the glass side, resulted in the same ENZ being measured.

The final structure etch process recipe was developed and carried out by The University of Florida's Nanoscale Research Facility. Plasma Enhanced Chemical Vapor Deposition (PECVD) was originally used to deposit the Si layer on to the ITO-onmetal substrates, however, the resultant growth was rough and spotty (as seen in 2.3). Electron-beam evaporation was ultimately used for Si growth on the ITO-onmetal substrates, motivated by success found in the literature [31]. The final sample consisted of twenty $100\mu m \times 100\mu m$ arrays, each separated by $500\mu m$. Each array had different Si, ITO pillar diameters, with a constant periodicity of 800nm from the center of one pillar to the center of a neighbor.

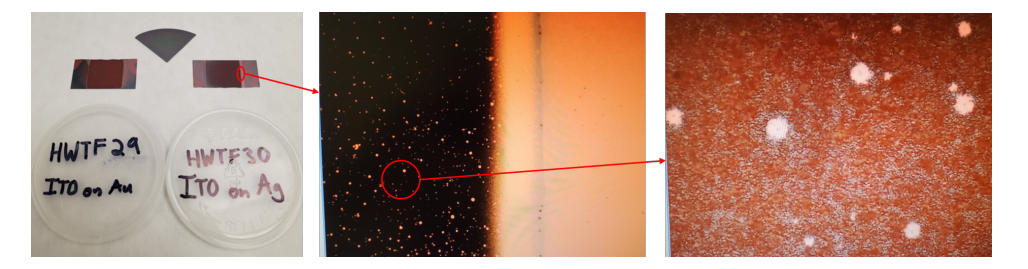


Figure 2.3: Rough Si growth on ITO-on-metal substrate using PECVD. Images supplied by UF Nanoscale Research Facility.

2.2.2 Linear Measurements

Linear reflectance measurements were performed using an optical microscope setup. A white light lamp source, coupled with a diffuser, was directed through 50:50 beam splitter and focused on to the sample using a 100x objective. To reduce the numerical aperture and increase the spot size, a pin hole was placed before the objective. The reflected light was collected using the same objective and sent through the emission path directed to an InGaAs detector for spectral analysis. A diagram of the described setup can be seen in Figure 2.4. The collected signal was normalized against a reference region on the same sample consisting of just gold.

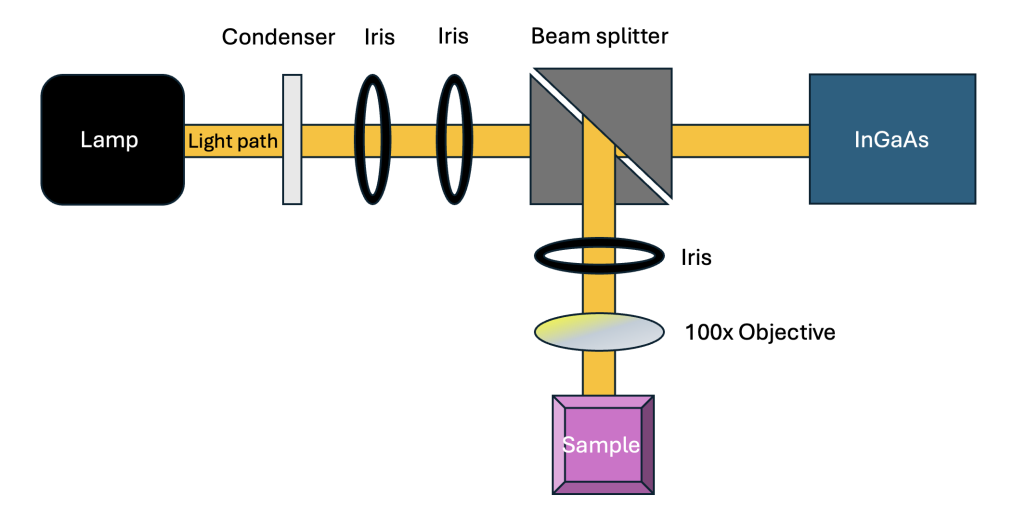


Figure 2.4: Diagram of linear optical path.

2.2.3 Nonlinear Measurements

Nonlinear measurements were performed using the same optical microscope set up, configured for femtosecond pulsed excitation. A Chameleon optical parametric oscillator (OPO) was pumped by a Chameleon Ultra II Ti:Sapphire femtosecond laser operating at a 80MHz repetition rate, was used to generate a tunable NIR pump light. The resultant beam was focused on to the sample using the same 100x objective. The reflected nonlinear signal passed through a KG5 short pass filter and directed to an InGaAs detector for spectral analysis. A diagram can be seen in Figure 2.5. The collected signal was normalized by accounting for all optical components including the objective lens, beam splitter, mirrors, short pass, lens, grating, iris, and the quantum efficiency of the detector.

Quality-factor (Q-factor) analysis was performed for each of the modes realized in the experimentally measured linear spectra. A MATLAB script was developed to identify the resonance minima and maxima through local extrema detection, allowing for tracking of the modes through the spectra sweep. The Q-factor was then calculated for each of the modes for different sample pillar diameters using $Q = \frac{\lambda_0}{FWHM}$, where the resonant wavelength was divided by the full width at half maximum of the resonance dip.

The conversion efficiency had to be estimated through calculations because a measured count-to-power ratio has not been experimentally measured for the required wavelength (404nm). The count-to-power ratio at 500nm was used to estimate the count-to-power ratio at 404nm. The raw counts for a pump excitation of 1215nm were fit with a gaussian, and the max count value was extracted and normalized by accounting for the mirrors, short pass, lenses, objective, beam splitter, iris, grating efficiency, and quantum efficiency of the detector.

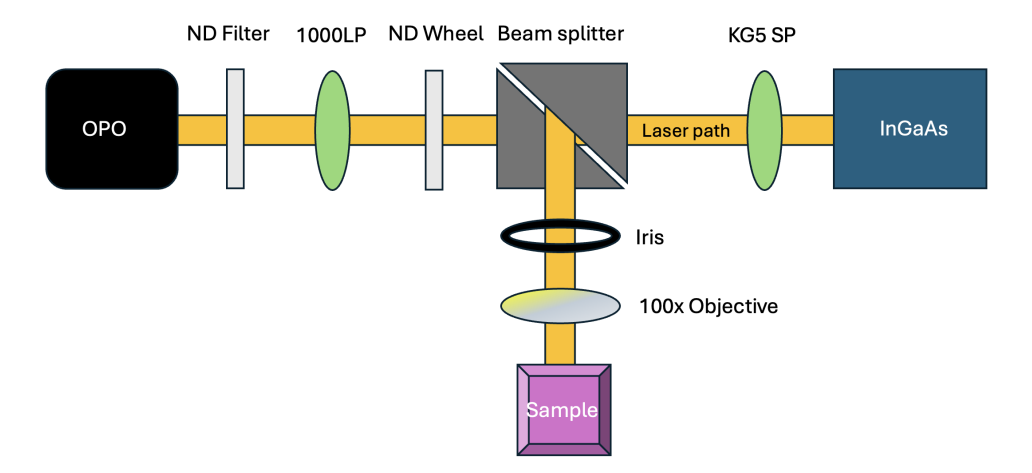


Figure 2.5: Diagram of nonlinear optical path.

2.2.4 Pump-Probe Measurements

To investigate the transient optical response of the structure, pump-probe measurements were performed. A Coherent Astrella consisting of a 5mJ amplified Ti:Sapphire setup was used as a pump source. The pump source has a repetition rate of 1kHz and a pulse duration of 35fs. The produced signal is split into one beam that is directed to the optical parametric amplifier (OPA) to be used as the system's pump, and a second beam that is delayed and focused incident on a sapphire crystal. The focused beam primarily induces self-phase modulation effects, resulting in the incident pulse spectrally broadening [8]. This spectral broadening produces a broadband white-light continuum, used as the probe beam. Polarization of the beams are s-polarized. The pump beam is incident on the sample at 30 and the probe beam at 5. Figure 2.6 shows a diagram of the described setup.

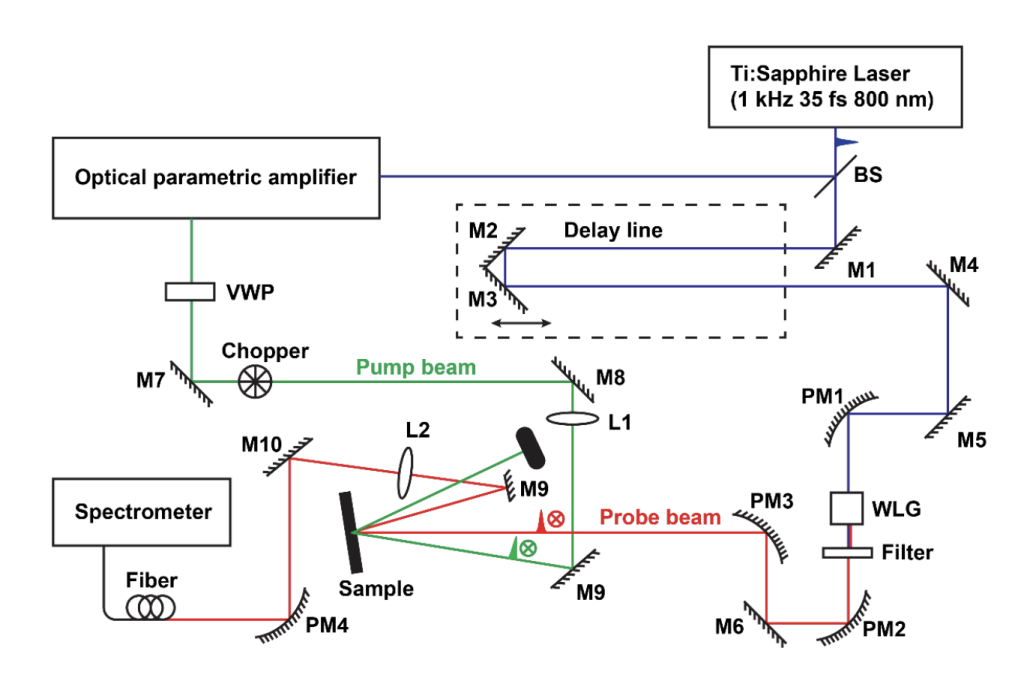


Figure 2.6: Diagram of pump-probe optical path. [54]

Chapter 3

Results

An SEM image of the final fabricated metasurface is shown in Figure 3.1c, the side profile illustration of the final structure is shown in Figure 3.1a, and the three-dimensional COMSOL structure can be seen in 3.1b. The correlation between the designed, simulated, and fabricated structure aligns well, with only minimal roughness on the fabricated gold mirror and silicon pillar side walls.

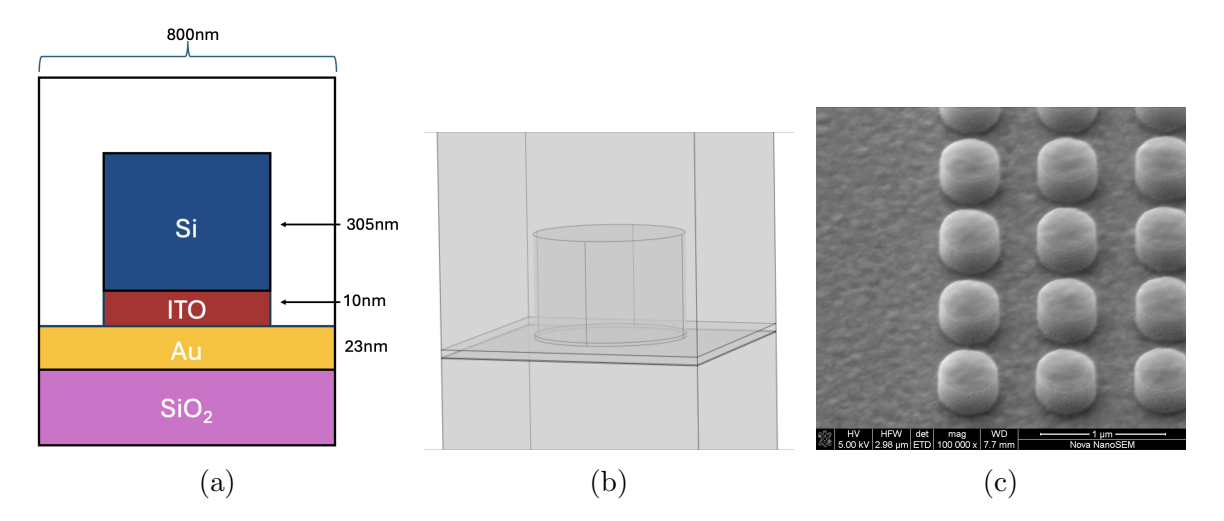


Figure 3.1: Au-dielectric Structure. (a) Side profile illustration of a single unit cell of the Au-dielectric structure. (b) Off-diagonal unit cell of simulated structure in COMSOL. (c) SEM image of final etched sample with gold back-reflector.

Due to the use of multiple simulation software within this project to simulate different calculations for the same structure, it is essential to determine the crossaccuracy between the two. Figure 3.2 shows a comparison between the simulated reflectance calculated using COMSOL Multiphysics and RETICOLO through MAT-LAB. The two simulation software show good agreement, allowing them to be used in tandem with little accuracy concerns.

Reflectance Comparison, 310nm Diameter

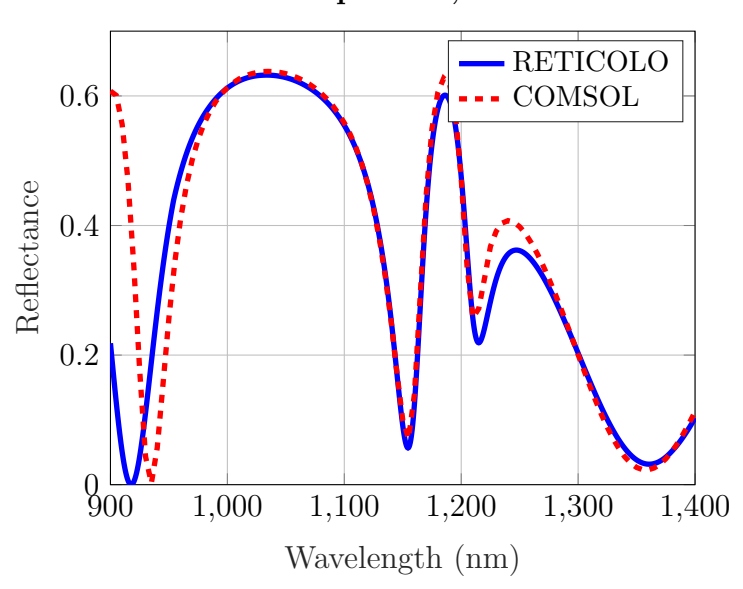


Figure 3.2: Comparison between MATLAB and COMSOL reflectance output for Si, ITO pillar on Au. Shows good agreement.

Figure 3.3a is the linear spectrum measured from the final sample. The diameter of the Si, ITO stacked pillar is swept along the x-axis and wavelength is plotted on the y-axis. Three central distinct modes can be seen. A top mode begins around $\lambda = 1080nm$ for a pillar diameter of 300nm, a middle mode begins at $\lambda = 900nm$ for a pillar diameter of 300nm, and a bottom mode begins at $\lambda = 900nm$ for a diameter of 380nm. To characterize the modes and determine where they come from, RETICOLO and COMSOL are used. Fitting methods discussed earlier were used to estimate the experimental ITO ENZ frequency, resulting in an approximate ENZ at 1000nm. Using the approximated ITO data, a reflectance sweep is produced (Figure 3.3b) showing similar top, middle, and bottom central modes. There is a grating mode around $\lambda = 1200nm$, that is not realized in the experimental results, likely due

to fabrication imperfections or interference.

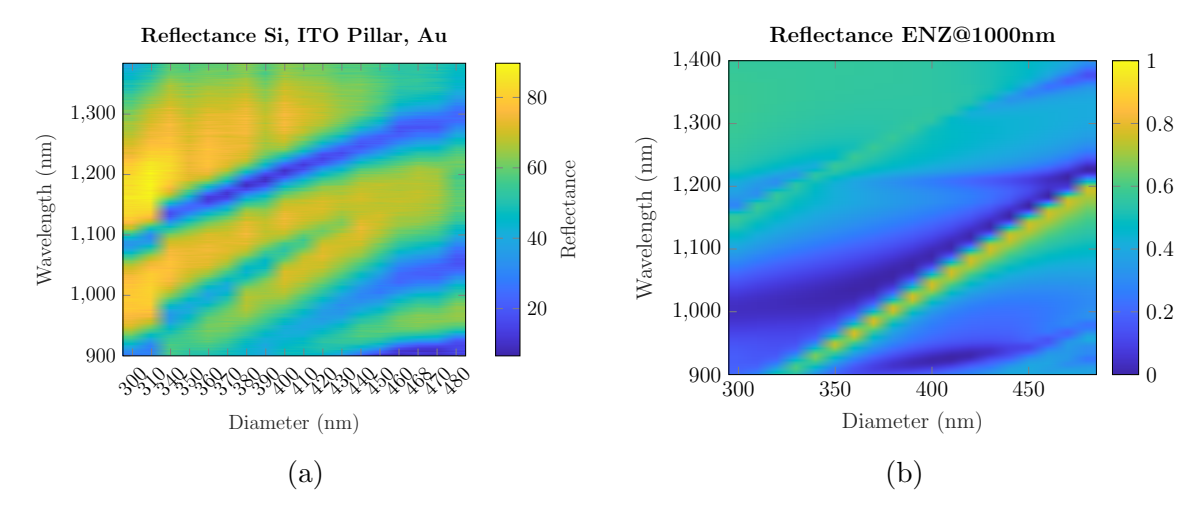


Figure 3.3: Experimental and Simulated Reflectance Sweeps: (a) Experimental reflectance measurements for Au-dielectric structure. (b) Simulated reflectance for Au-dielectric structure, with ITO ENZ at 1000nm.

To shed some initial light on the modes observed in the experimental and simulation reflectance spectra, additional reflectance spectra for the metasurface were simulated with varying ITO ENZ frequencies. Figure 3.4 shows the comparison between these sweeps. Two modes corresponding to the top and middles modes identified in Figure 3.3a can be seen in the same location across all of the sweeps, with a third broader mode shifting throughout. This third mode is observed as the bottom mode in Figure 3.3b. The lack of change shown in the top and middle modes indicate that they're likely formed from a geometry-related condition, while the bottom mode is likely related to a material property of the ITO.

Using Figure 3.3b as a guide, COMSOL Multiphysics was used to simulate individual diameter cuts of the metasurface, and probe at resonant wavelengths to investigate the electric field distributions of each resonance mode. Figure 3.5 shows the electric field distributions at different wavelengths for a stacked gold, ITO pillar diameter of 450nm. Figure 3.5d is the electric field distribution for the grating mode present across the diameters; showing distinct signs of such a mode in the glass substrate layer. A clear electric dipole within the silicon pillar is shown in Figure 3.5c.

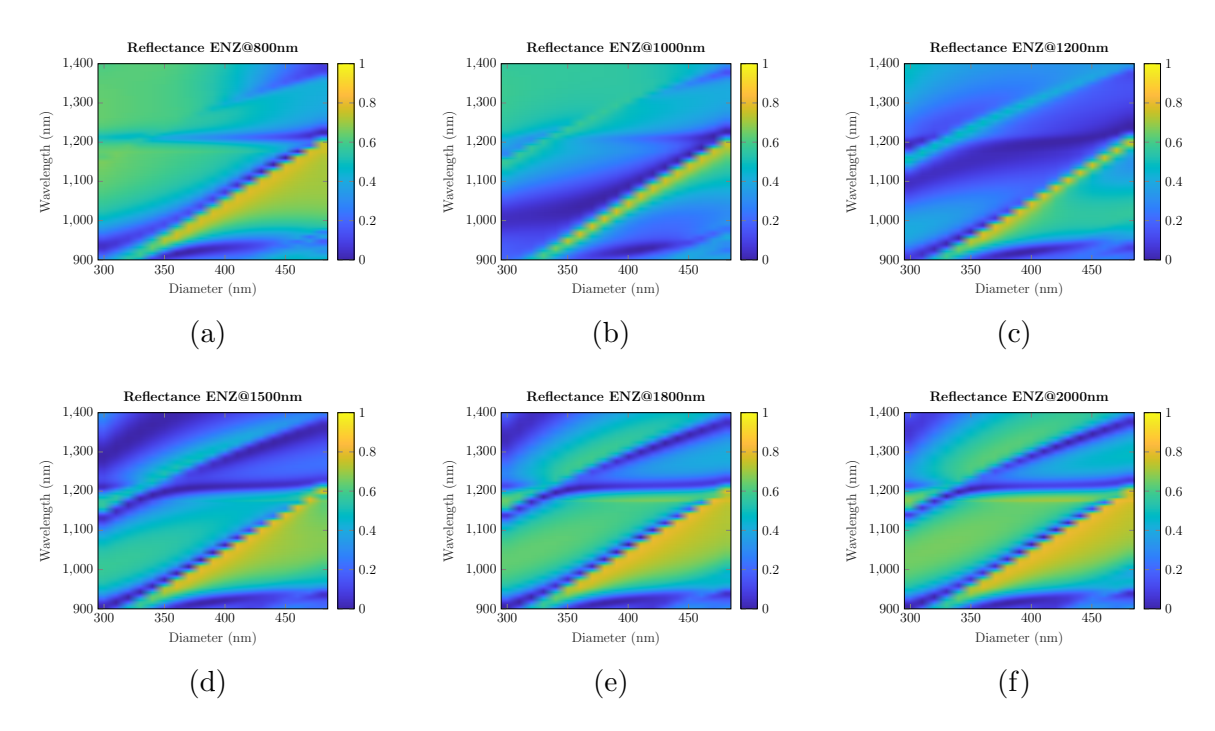


Figure 3.4: ITO ENZ Sweep Comparison. (a) ENZ at 800 nm. (b) ENZ at 1000 nm. (c) ENZ at 1200 nm. (d) ENZ at 1500 nm. (e) ENZ at 1800 nm. (f) ENZ at 2000 nm.

with some periodic signals in the glass substrate, likely due to slight coupling to the grating mode. Figure 3.5e shows a magnetic dipole within the silicon pillar. Across all field distributions, strong electric fields are observed within the ITO pillar.

As mentioned earlier in this work, a similar structure was theoretically explored for realizing BICs [45]. Similar modes were found in both works, so their mode analysis can be applied to analyzing the modes found in Figure 3.3a. The top mode is a magnetic dipole hybrid mode arising from the silicon pillar coupling to its mirror image and to the ITO pillar, effectively directing the generated field from the silicon pillar, mirror image coupling into the ITO pillar. The middle hybrid mode is the product of coupling between the silicon pillar, ITO pillar, and the gold thinfilm. Lastly, the bottom resonance is the Berreman mode arising from the ITO pillar.

Figure 3.6 helps to further shed light on modal creation by showing the electric field strengths present in the ITO and silicon pillars separately within the spectra.

3.6b shows moderately strong electric fields within the ITO pillar around the region of

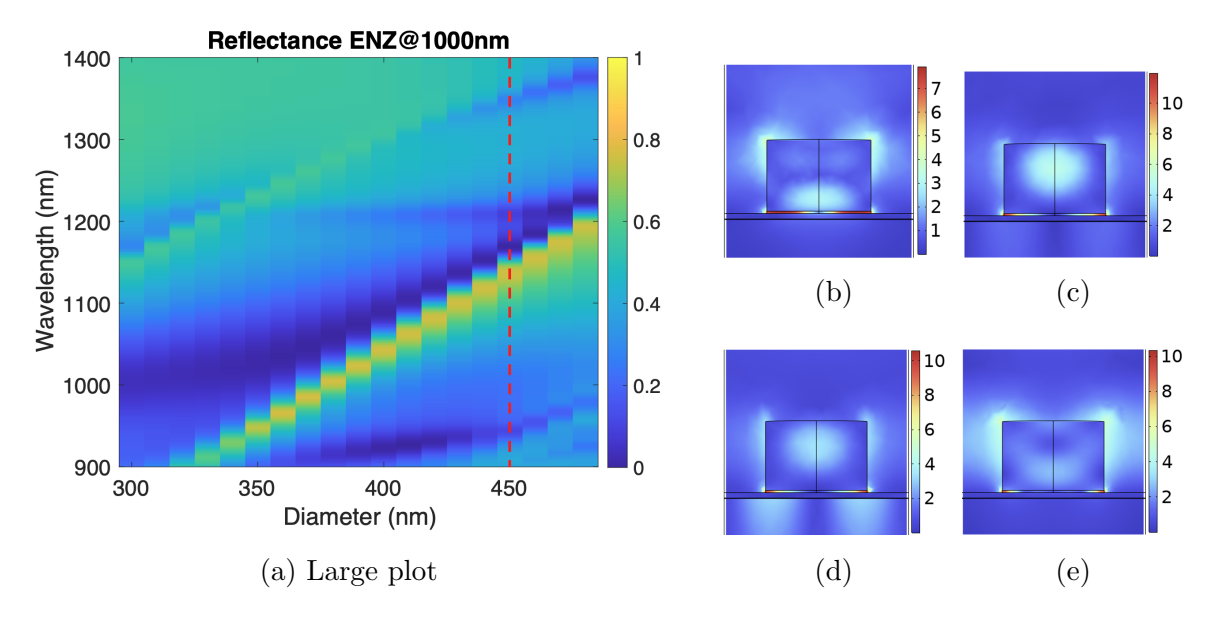


Figure 3.5: Electric field distribution probing in xz plane, normalized to the incident plane wave: (a) Simulated reflectance sweep for ENZ at 1000nm, dotted red line shows cut at a diameter of 450nm for which electric field distributions were calculated. (b) Magnitude of electric field distribute at $\lambda = 985nm$. (c) Magnitude of electric field distribute at $\lambda = 1190nm$. (d) Magnitude of electric field distribute at $\lambda = 1205nm$. (e) Magnitude of electric field distribute at $\lambda = 1350nm$.

the top mode, further indicating the ITO's available electric field strength for coupling to the magnetic dipole, mirror image.

Quality-factor (Q-factor) analysis was performed on the experimental data to determine if a BIC was present in one of the three modes, as described in the experimental methods section. Figure 3.7 shows the Q-factor results for the experimental reflectance data, with diverging Q-factor behavior occurring in the middle mode. This increase in Q-factor aligns well with reported behavior observed around BICs [45, 53, 17, 44]. Further electric field dispersion analysis through simulations are needed to further confirm the presence of the BIC.

Nonlinear measurements were performed to investigate the third-harmonic generation (THG) of the metasurface. The strongest THG response was measured for the metasurface with a pillar diameter of 420nm. Excitation pump wavelength is tuned from 1055nm to 1395nm at 15nm intervals. THG counts are strongest at the top

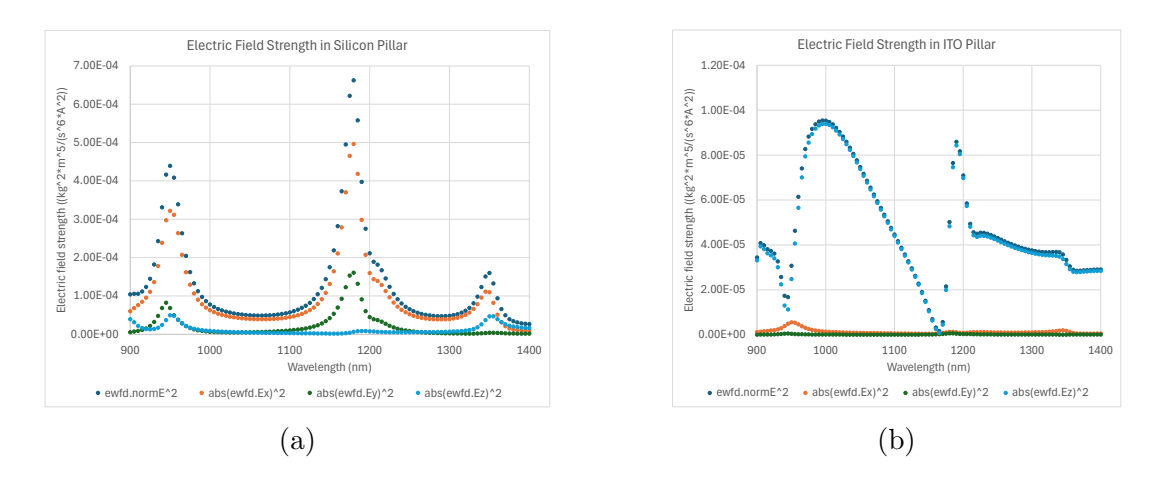


Figure 3.6: Electric field strengths in the silicon and ITO pillars. (a) Silicon pillar. (b) ITO pillar.

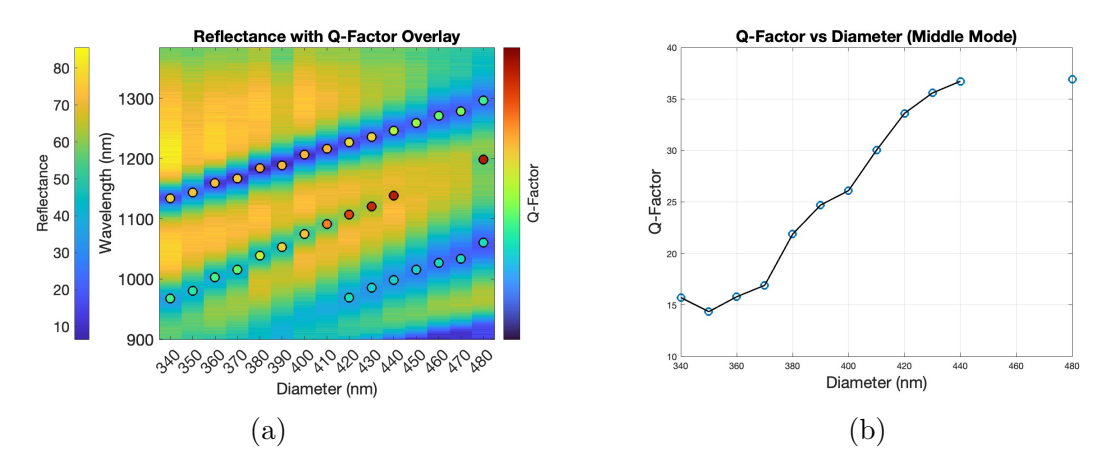


Figure 3.7: Q-factor analysis: (a) Q-factor overlay for top, middle, and lower reflectance mode. (b) Q-factor diverging for middle mode.

resonance, specifically when pumped on resonance, and decrease as the excitation pump wavelength moves off resonance. The THG counts are significantly lower for the middle resonance. The lowest mode fell outside the range of excitation.

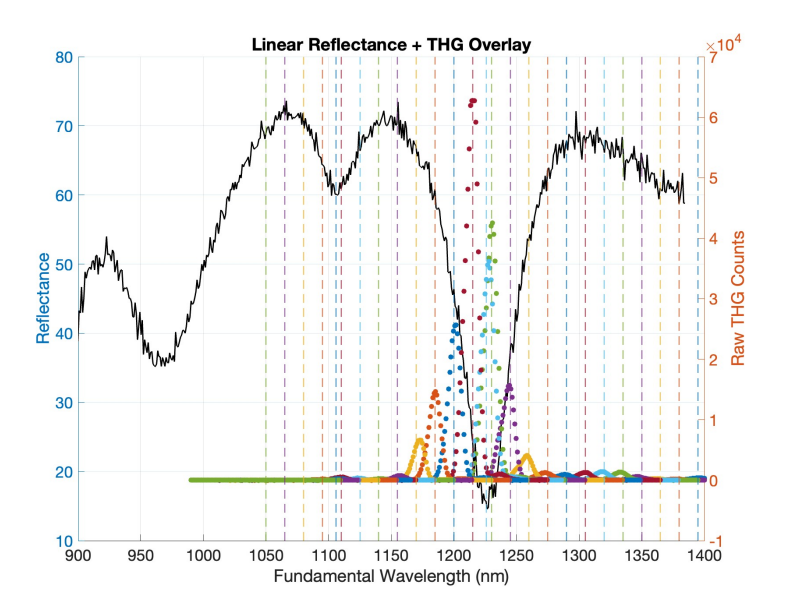


Figure 3.8: Raw THG counts normalized to background, for changing excitation pump wavelength. The linear reflectance (black line) is overlaid with raw THG data, and the different excitation pump wavelengths (dashed vertical color lines). Highest raw THG counts occurring with pump wavelength of 1215nm. Pillar diameter is 420nm.

The conversion efficiency was calculated for the highest THG signal using estimations described in experimental methods. The estimated normalized conversion efficiency is $4.18 \times 10^{-9} W^{-2}$. This estimated conversion efficiency is expected to change when experimentally measured; however, it is expected to be an underestimate of the actual conversion efficiency.

Lastly, pump-probe measurements were performed to study the temporal dynamics of the system. The metasurface with a pillar diameter of 420nm was focused on due to it exhibiting the highest THG signals. The sample was pumped with a wavelength of 1400nm, to ensure it wasn't pumped on resonance, with a power of $13\mu W$. Figure 3.9 shows the spectra results. A long process occurs around 1200nm, corresponding to the high THG producing mode. The longer length of this mode is

unusual, and doesn't occur in previously reported results for a similar metasurface not containing an ENZ material [54], indicating that its origin is likely due to the presence of the ITO in the system. A shorter response is seen around 1250nm, likely related to a two-photon absorption process.

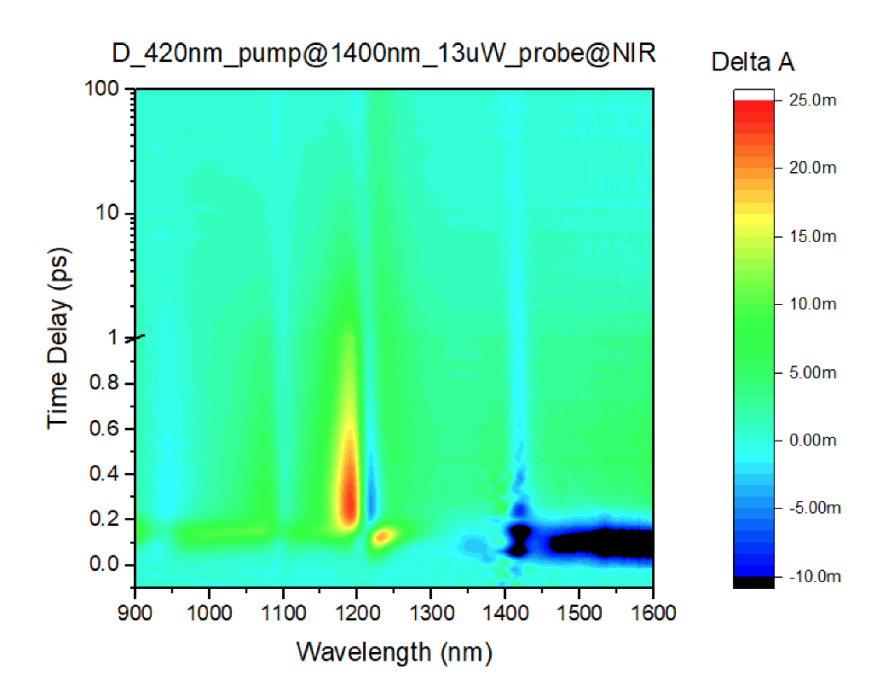


Figure 3.9: 2D map of absorption spectra change (ΔA) as a function of the time delay between the pump and probe and the probe wavelength.

These time scales were further investigated by looking at the kinetic cuts shown in Figure 3.10. Figure 3.10a shows an initial fast peak in ΔA followed by a slower response that decays over more than 100ps. Figure 3.10b shows the ΔA dip feature that occurs mirroring the peak shown in Figure 3.10a. It too features a fast initial response that is followed by a slow response lasting over 100ps.

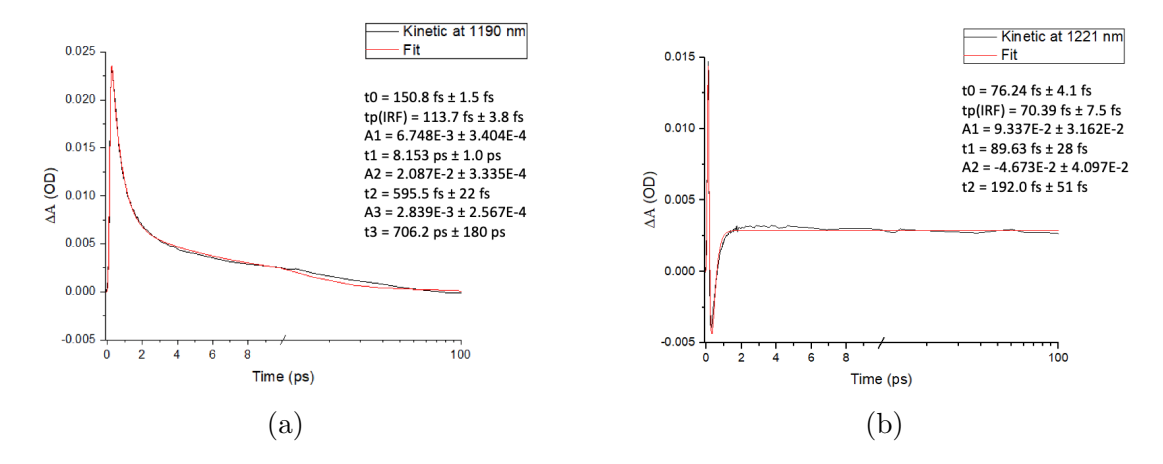


Figure 3.10: Kinetic cuts: (a) Cut at 1190nm. (b) Cut at 1221nm.

Chapter 4

Conclusion and Next Steps

We have experimentally demonstrated the impact of integrating ENZ materials into metasurfaces, realizing a significant enhancement of third harmonic generation (THG) signals and distinct temporal dynamics compared to similar structures lacking ENZ materials. The estimated normalized THG conversion efficiency achieved in this work, $4.18 \times 10^{-9} W^{-2}$, is over two orders of magnitude higher than non-ENZ material containing systems. The analysis of the time-resolved measurements show a distinct slower mode, likely due to ITO's carrier kinetics near the ENZ wavelength.

This project set out to investigate if leveraging the tunability and field enhancement characteristics of ENZ materials in a metasurface could result in nonlinear enhancement and show that it was due to the ENZ material. We have shown through combining simulation and experimental data, that strong field confinement in the ITO layer occurs at resonant modes producing enhanced THG signals, with a distinct slow in carrier dynamics at the wavelength of interest. These results clearly show the role that the ENZ material plays in the system.

Our findings further bolster the importance of ENZ materials in the field of nanophotonics and nonlinear optics. However, we are left with several limitations and open questions. An experimentally calculated count-to-power ratio needs to be determined to allow a true, un-estimated, conversion efficiency to be found, and further research into the mode formation should be performed to better understand exactly the modes form and why the upper mode produces such high THG signals. Investigating the impact of combining this ENZ metasurface with a tunable BIC could be advantageous for further enhancement, but will require better understanding of tuning the ITO ENZ while on metal. This will have the added bonus of allowing for more accurate simulations, and in turn more accurate mode characterization. Further pump-probe measurements should be performed, pumping at a different wavelength to ensure the 1400nm pump wavelength used in this work isn't pumping on a unseen mode and impacting results.

Bibliography

- [1] M Zahirul Alam, Israel De Leon, and Robert W Boyd. "Large optical nonlinearity of indium tin oxide in its epsilon-near-zero region". In: *Science* 352.6287 (2016), pp. 795–797.
- [2] Klaus-Jürgen Bathe. "Finite element method". In: Wiley encyclopedia of computer science and engineering (2007), pp. 1–12.
- [3] Nils Bernhardt et al. "Quasi-BIC resonant enhancement of second-harmonic generation in WS2 monolayers". In: *Nano Letters* 20.7 (2020), pp. 5309–5314.
- [4] DW Berreman. "Infrared absorption at longitudinal optic frequency in cubic crystal films". In: *Physical Review* 130.6 (1963), p. 2193.
- [5] Bhairov Kumar Bhowmik et al. "High-quality factor Quasi-BIC mode via selective symmetry-breaking approach in a terahertz metasurface". In: New Journal of Physics 26.6 (2024), p. 063024.
- [6] Robert W Boyd. "Material slow light and structural slow light: similarities and differences for nonlinear optics". In: Journal of the Optical Society of America B 28.12 (2011), A38–A44.
- [7] Robert W Boyd, Alexander L Gaeta, and Enno Giese. "Nonlinear optics". In: Springer Handbook of Atomic, Molecular, and Optical Physics. Springer, 2008, pp. 1097–1110.

- [8] Anne-Laure Calendron et al. "White-light generation with sub-ps pulses". In: Optics express 23.11 (2015), pp. 13866–13879.
- [9] Salvatore Campione, Igal Brener, and Francois Marquier. "Theory of epsilon-near-zero modes in ultrathin films". In: *Physical Review B* 91.12 (2015), p. 121408.
- [10] Salvatore Campione, Igal Brener, and Francois Marquier. "What is an epsilon-near-zero mode?" In: Advanced Photonics 2015. Optica Publishing Group, 2015, IM4A.5. DOI: 10.1364/IPRSN.2015.IM4A.5. URL: https://opg.optica.org/abstract.cfm?URI=IPRSN-2015-IM4A.5.
- [11] Aqing Chen et al. "A new investigation of oxygen flow influence on ITO thin films by magnetron sputtering". In: Solar energy materials and solar cells 120 (2014), pp. 157–162.
- [12] lecture 16 slides on "Third-order nonlinear susceptibility $\chi^{(3)}$ and its tensor.".
- [13] Adam D Dunkelberger et al. "Ultrafast active tuning of the Berreman mode". In: ACS Photonics 7.1 (2019), pp. 279–287.
- [14] Dhruv Fomra et al. "Nonlinear optics at epsilon near zero: From origins to new materials". In: *Applied Physics Reviews* 11.1 (2024).
- [15] H Friedrich and D Wintgen. "Interfering resonances and bound states in the continuum". In: *Physical Review A* 32.6 (1985), p. 3231.
- [16] Lihong Gao, F Lemarchand, and Michel Lequime. "Refractive index determination of SiO2 layer in the UV/Vis/NIR range: spectrophotometric reverse engineering on single and bi-layer designs". In: Journal of the European Optical Society-Rapid publications 8 (2013), p. 13010.
- [17] Yixiao Gao, Lei Xu, and Xiang Shen. "Q-factor mediated quasi-BIC resonances coupling in asymmetric dimer lattices". In: *Optics Express* 30.26 (2022), pp. 46680–46692.

- [18] B Harbecke, B Heinz, and P Grosse. "Optical properties of thin films and the Berreman effect". In: *Applied Physics A* 38 (1985), pp. 263–267.
- [19] Niels JJ van Hoof et al. "Unveiling the symmetry protection of bound states in the continuum with terahertz near-field imaging". In: ACS photonics 8.10 (2021), pp. 3010–3016.
- [20] Sebastian P Horvath et al. "Slow light frequency reference cavities—proof of concept for reducing the frequency sensitivity due to length fluctuations". In: New Journal of Physics 24.3 (2022), p. 033034.
- [21] Henry Howell. "Enhancing Optical Resonance Modulation using Indium Tin Oxide and Bound States in the Continuum". Unpublished, turned in document as research and literature report to Emory Physics department to fullfill second year requirements. PI: Hayk Harutyunyan.
- [22] Chia Wei Hsu et al. "Bound states in the continuum". In: *Nature Reviews Materials* 1.9 (2016), pp. 1–13.
- [23] Chia Wei Hsu et al. "Observation of trapped light within the radiation continuum". In: *Nature* 499.7457 (2013), pp. 188–191.
- [24] Jean Paul Hugonin and Philippe Lalanne. "Reticolo software for grating analysis". In: arXiv preprint arXiv:2101.00901 (2021).
- [25] Jacob B Khurgin. "Slow light in various media: a tutorial". In: Advances in Optics and Photonics 2.3 (2010), pp. 287–318.
- [26] Nathaniel Kinsey et al. "Near-zero-index materials for photonics". In: *Nature Reviews Materials* 4.12 (2019), pp. 742–760.
- [27] Alexander Korneluk, Julia Szymczak, and Tomasz Stefaniuk. "Annealing-free fabrication of high-quality indium tin oxide films for free-carrier-based hybrid metal—semiconductor nanophotonics". In: *Scientific Reports* 13.1 (2023), p. 18520.

- [28] Kirill Koshelev et al. "Nonlinear metasurfaces governed by bound states in the continuum". In: Acs Photonics 6.7 (2019), pp. 1639–1644.
- [29] Ka Kin Lam et al. "Effect of Thickness on the Optical and Electrical Properties of ITO/Au/ITO Sandwich Structures". In: ACS Applied Materials & Interfaces 12.11 (2020). PMID: 32088951, pp. 13437-13446. DOI: 10.1021/acsami.9b20203. eprint: https://doi.org/10.1021/acsami.9b20203. URL: https://doi.org/10.1021/acsami.9b20203.
- [30] Kuen Yao Lau et al. "Tunable optical nonlinearity of indium tin oxide for optical switching in epsilon-near-zero region". In: Nanophotonics 11.18 (2022), pp. 4209–4219.
- [31] Cheng Li et al. "ITO/Si/ITO semi-cone-shell chiral complexes on silicon nanocones with broadband circular dichroism in the mid-infrared wavelength". In: *Optics Express* 30.22 (2022), pp. 40925–40935.
- [32] Chentao Li et al. "Invertible optical nonlinearity in epsilon-near-zero materials".

 In: *Physical Review Research* 5.1 (2023), p. 013198.
- [33] Shiyu Li et al. "Symmetry-protected bound states in the continuum supported by all-dielectric metasurfaces". In: *Physical Review A* 100.6 (2019), p. 063803.
- [34] Franz JF Löchner et al. "Polarization-dependent second harmonic diffraction from resonant GaAs metasurfaces". In: Acs Photonics 5.5 (2018), pp. 1786– 1793.
- [35] Qijing Lu, Ziyao Feng, and Xiankai Sun. "Symmetry-protected bound states in the continuum on an integrated photonic platform". In: *Nanophotonics* 13.18 (2024), pp. 3527–3534.
- [36] Ting S Luk et al. "Enhanced third harmonic generation from the epsilon-near-zero modes of ultrathin films". In: *Applied Physics Letters* 106.15 (2015).

- [37] Momchil Minkov and Vincenzo Savona. "Wide-band slow light in compact photonic crystal coupled-cavity waveguides". In: *Optica* 2.7 (2015), pp. 631–634.
- [38] Gianni Q Moretti et al. "Si metasurface supporting multiple quasi-BICs for degenerate four-wave mixing". In: *Nanophotonics* 13.18 (2024), pp. 3421–3428.
- [39] COMSOL Multiphysics. Detailed explaination of the Finite Element Method (FEM). 2016.
- [40] J v. Neumann. "Über die analytischen Eigenschaften von Gruppen linearer Transformationen und ihrer Darstellungen". In: *Mathematische Zeitschrift* 30.1 (1929), pp. 3–42.
- [41] Ward D Newman et al. "Ferrell–Berreman modes in plasmonic epsilon-near-zero media". In: *Acs Photonics* 2.1 (2015), pp. 2–7.
- [42] Gennadiy P Nikishkov. "Introduction to the finite element method". In: *University of Aizu* (2004), pp. 1–70.
- [43] Natalie Rozman, Kebin Fan, and Willie J Padilla. "Symmetry-broken high-Q terahertz quasi-bound states in the continuum". In: Acs Photonics 11.5 (2024), pp. 1893–1900.
- [44] Yuhang Ruan et al. "Strong resonance response with ultrahigh quality factor in grating-multilayer systems based on quasi-bound states in the continuum".

 In: Scientific Reports 12.1 (2022), p. 21471.
- [45] Wenjuan Shi et al. "Enhanced optical nonlinearity of epsilon-near-zero metasurface by quasi-bound state in the continuum". In: *Materials Today Nano* 26 (2024), p. 100474.
- [46] Manuel E Solano et al. "Comparison of rigorous coupled-wave approach and finite element method for photovoltaic devices with periodically corrugated metallic backreflector". In: *Journal of the Optical Society of America A* 31.10 (2014), pp. 2275–2284.

- [47] Anna Sytchkova et al. "Optical, structural and electrical properties of sputtered ultrathin chromium films". In: *Optical Materials* 121 (2021), p. 111530.
- [48] Félix Thouin et al. "Field Enhancement and Nonlocal Effects in Epsilon-Near-Zero Photonic Gap Antennas". In: ACS nano 19.8 (2025), pp. 7996–8004.
- [49] Simon Vassant et al. "Berreman mode and epsilon near zero mode". In: *Optics express* 20.21 (2012), pp. 23971–23977.
- [50] Wen-Fa Wu and Bi-Shiou Chiou. "Effect of oxygen concentration in the sputtering ambient on the microstructure, electrical and optical properties of radio-frequency magnetron-sputtered indium tin oxide films". In: Semiconductor science and technology 11.2 (1996), p. 196.
- [51] Peng Xie et al. "Strong coupling of resonant metasurfaces with epsilon-near-zero guided modes". In: *Nano Letters* 24.29 (2024), pp. 9027–9033.
- [52] Lei Xu et al. "Enhanced four-wave mixing from multi-resonant silicon dimerhole membrane metasurfaces". In: New Journal of Physics 24.3 (2022), p. 035002.
- [53] Guoce Yang et al. "Optical bound states in the continuum enabled by magnetic resonances coupled to a mirror". In: *Nano Letters* 22.5 (2022), pp. 2001–2008.
- [54] Guoce Yang et al. "Unlocking efficient ultrafast bound-electron optical non-linearities via mirror induced quasi bound states in the continuum". In: Nano Letters 24.5 (2024), pp. 1679–1686.
- [55] Vladimir A Zakharov and Alexander N Poddubny. "Transverse magneto-optical Kerr effect enhanced at the bound states in the continuum". In: *Physical Review* A 101.4 (2020), p. 043848.
- [56] Yixuan Zeng et al. "Manipulating Light with Bound States in the Continuum: from Passive to Active stems". In: Advanced Optical Materials 12.25 (2024), p. 2400296.

[57] Huifang Zhang et al. "High-efficiency dielectric metasurfaces for polarization-dependent terahertz wavefront manipulation". In: Advanced Optical Materials
 6.1 (2018), p. 1700773.